Master Thesis

Review of halo measurements at the Large Hadron Collider with collimator scans

Author:
Paola Racano

Supervisor:
Prof. Andrea Mostacci
Dr. Hector Garcia Morales
Dr. Stefano Redaelli

Master of Science in Electronic Engineering
Department of Information Engineering, Electronics and Telecommunications

January 5, 2019

"Extreme suffering is a beloved thing
on the path of carnage"

Eiichirō Oda

UNIVERSITÀ DEGLI STUDI DI ROMA "LA SAPIENZA"

Abstract

Faculty of Information Engineering, Informatics and Statistics
Department of Information Engineering, Electronics and Telecommunications

Master of Science in Electronic Engineering

Review of halo measurements at the Large Hadron Collider with collimator scans

by Paola RACANO

A good modeling of the beam distribution is essential in order to understand limitiations from over-populated tails in high-power particle accelerators and find the best strategy to clean particles in the tails, that may cause damage to the accelerator components. Therefore the beam profile in the transverse plane at the Large Hadron Collider (LHC) using collimator scans was measured, analysed and discussed. Two models, Double Gaussian and Lèvy Student, were investigated in order to understand which one fits better the shape of the beam reconstructed from the signal of the Beam Loss Monitor (BLM) during beam scraping with LHC collimaotr and through the Beam Wire Scanner (BWS). A series of Python-based scripts were developed to analuse measurements data, to fit the obtained profiles and to compare the parameters obtained from the fit with both models and to evaluate the particles content in the tail region. This work demonstrated that is possibile to use these two models to represent the beam profile in the vertical and horizontal planes respectivley. A set of reference fit paramters was collected, that allows to model the LHC transverse beam distributions in the cases considerated. A systematic analysis for various measurements performed at the LHC was carried out and is also presented.

Acknowledgements

First of all, I would like to thank my supervisor Dr. Stefano Redaelli for allowing me to be part of the CERN BE-ABP/HSS department, for his supervisioning and help during the redaction of this report.

I would like to thank Dr. Hector Garcia Morales and Dr. Massimo Giovannozzi for their constant supervisioning and patience, for providing me knowledge about particle accelerators and for all the fruitful discussions held throughout this period. In particular, I would like to thank Dr. Garica Morales for his availability whenever I knocked at his door, for all the clarifications provided and for encouragement whenever difficulties were encountered.
I am also very grateful to Dr. Alessio Mereghetti for his unconditional help during all the period of my stay at CERN.

Also, I want to thank my supervisor at the University of Rome "La Sapienza", Prof. Andrea Mostacci, for introducing me to the world of particle accelerators, for providing me the unique opportunity to collaborate with CERN and for supervising my work from my home institute.

A substantial thank goes to my parents for their support over all these years, for all the advice you gave me, for spurred me, for your patience, for all the sacrifices you have made to allow me to be here. It would have been impossible for me to reach this stage without your encouragement. Thank you!
I would like also to thank my sisters, Andrea and Pier for coming in Switzerland, bringing a little taste of home. Thank you for all the nights you spent with me at home, because full of books to study, just to have even a quick dinner together. Thanks for simplifying things when I was nervous about the exams, always worried about me and finding a way to cheer me up when everything seemed to go wrong.
Thanks to Rosa Maria and Giuliano, for the encouragement, availability and affection shown in all these years, thank you for everything you have done.

I would like to thank all those with whom I spent these university years, making them more enjoyable.
I would like to thank Sandro, for all the times you dragged me out of the house and for those where you stayed at home with me just to make me amuse.
A thank goes also to those who, for six months, have been my new family in Switzerland, thanks for all the barbecues and beers, for welcoming me at home, any time of any day, for all the moments spent together, for not having me made to feel lonely away from home.

A huge thank goes to you, that, unfortunately, have had to undergo all my mood swings. Thank you for the infinity of kilometers made, for always looking for a way to help me and reassure me, for not leaving me alone during the post-dinner study, that often lasted until the morning. Thanks for always being a point of reference, thanks because despite everything you remained at my side.

Contents

List of Figures

List of Tables

Dedicated to my family

Introduction

The Large Hadron Collider (LHC) at CERN was designed to accelerate and store particle beams of intensities up to 3×10^{14} protons at a particle momentum of 7 TeV/c. This corresponds to a stored beam energy of 360 MJ, which has to be handled in the superconducting magnet system environment of the LHC. Less than a billionth of the total beam energy would be sufficient to cause the superconducting magnets to quench.
Therefore, beam distribution profile plays a key role in the LHC. In general, Gaussian profiles are assumed for the beam distribution but it is well known that beam tails are usually overpopulated due to different physical mechanisms. These tail particles may create uncontrolled losses that can damage components, cause magnets to quench and increase the experimental back-ground. Therefore, a good modeling of the beam distribution is essential in order to understand the impact on the operation and to find the best strategy for cleaning these particles. Knowing the real shape of the beam in the LHC is important to identify limitations of future machine upgrades with respect to machine protection requirements. In particular, this is important for the *High-Luminosity* upgrade of the LHC (*HL-LHC*), that aims at doubling the beam intensity, in which crab cavites will be used to rotate the beam. Crab cavites help to increase the number of collisions that occur in a given amount of time. In fact, what makes them special is their ability to "tilt" the bunches in each beam, maximising their overlap at the collision point. It is therefore interesting to be able to find a valid mathematical model, which can effectively fit the beam profile. Furthermore, in this new operational mode, it is also important to know the initial transverse beam population profile.
To precisely reconstruct the transverse beam profiles, different beam scrapings using collimators have been performed at two different stages of the LHC cycle, at 450 GeV and at 6 TeV. The measurements have been carried out in the transverse plane, through the use of collimator jaws. The particles are scraped by moving into the beam the collimator jaws with small steps, and the beam losses are recorded by beam loss monitors (BLM) close to the collimators used. From the beam loss signal generated, the fraction of scraped particles has been evaluated. This information, combined with the collimator postions, allowed the reconstruction of the beam profile in the transveral plane. In order to have a benchmark, measurements with the Beam Wire Scanner (BWS) have also been carried out. This instrument has also allowed the extraction of some parameters, useful for the reconstruction of the beam profile. In order to find a suitable mathematical model to describe the measured beam profile, two models have been applied to the same data sets and were systematically compared.
In this work, after a brief introduction on the LHC and its collimation system, the theoretical background on the basic accelerator physics concepts relevant for the study of the beam profile in the transverse plane is introduced. It proceeds with the introduction of the instrumentation used to perform the analysis, paying particular attention to the effects of scraping on the BLM signal. Subsequently there is

an explanation of the script implemented to analyze the data, in which a block diagram of it is shown and the main functions implemented to achieve the objective are examined in depth. Finally, the results obtained are shown, and the most relevant considerations are highlighted, from which the conclusions were then extracted.

Chapter 1

The LHC and the Collimation System

The Large Hadron Collider (LHC) at the European Organization for Nuclear Research (CERN) in Geneva, built between 1998 and 2008, is the world's largest and most powerful particle accelerator.
The first beam was circulated through the collider on the morning of 10 September 2008. A few days later, an electrical fault led to a damage of some components of the accelerator, which were repaired during the winter shutdown. On 20 November 2009, low-energy beams circulated in the tunnel for the first time since the incident, and shortly after, the LHC achieved 1.18 *TeV* per beam to become the world's highest-energy particle accelerator. The early part of 2010 saw the continued ramp-up of beam in energies and on 30 March 2010, the LHC set a new record for high-energy collisions by colliding proton beams at a combined energy level of 7 *TeV* (3.5 *TeV* per beam). On the 2012, after the winter shutdown, the first collisions with stable beams was performed and the energy was increased to 4 *TeV* per beam (8 *TeV* in collisions). During this year the first discovery of new elementary particle happened: a new boson observed that was "consistent with" the theorized Higgs boson. On February 2013 begun the first long shutdown during which upgrades were done to safely handle the current required for 7 TeV per beam (14 TeV). This marked the end of the first operational run (*Run 1*).
On 5 April 2015, the LHC restarted and both beams circulated in the collider. Few days later, a new record energy of 6.5 *TeV* per beam was achieved, which became the operating energy for 2015 to 2017.
The study that is presented is this thesis has been done during the last period of the second operational run (*Run 2*), just before the long shutdown scheduled for December 2018.

1.1 LHC Layout

The LHC is a circular particle accelerator with a 26.659 km long circumference situated at the border between Switzerland and France at a depth ranging from 50 to 175 metres underground. The basic layout of the LHC is formed by eight arcs and eight straight sections, the so-called Interaction Regions (IRs), where the four main experiments are placed - ATLAS, CMS, ALICE and LHCb [Bracco, 2009].
An overview of the LHC layout is given in Figure 1.1.

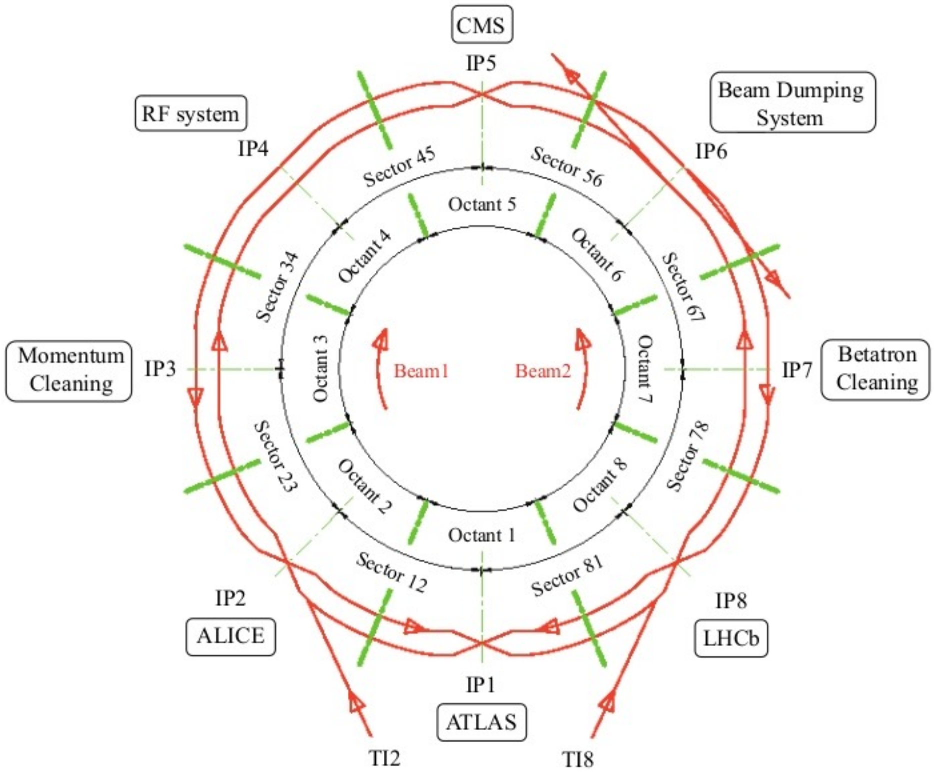

FIGURE 1.1: The basic layout of the Large Hadron Collider (LHC). Beam 1 circulates clockwise and Beam 2 counter-clockwise.

The two particle beams are injected into the machine in IR2 (Beam 1) and IR8 (Beam 2) respectively at an energy of 450 GeV and accelerated up to the nominal top energy (7 GeV) by the RF cavities located in IR4. The beams travel at close to the speed of light in opposite directions in two separate beam pipes, kept at ultrahigh vacuum, and they are guided around the accelerator ring by a strong magnetic field maintained by superconducting electromagnets.
When an electrically charged particle moves through a constant magnetic field, it moves in a circular path. The bending radius depends on both the strength of the magnets and the energy of the beam. If the energy increases, the ring becomes larger, while if the strength of the magnets increases, the ring becomes smaller. The LHC is an accelerator, and as such it increases the energy of particles in the beam. Since the size of the ring is fixed, the streght of the magnets must be increased when the energy of the beam increases.
In this regard, an important figure of merit is the *magnetic rigidity*, which is a measure of the momentum of the particle, and it refers to the fact that a higher momentum particle will have a higher resistance to deflection by a magnetic field. It is defined as:

$$B\rho = \frac{p}{e} \tag{1.1}$$

where B is the magnetic field, ρ is the bending radius, p is the the particle momentum and e is its charge.
We must keep in mind that when an electric current runs through a wire, it creates a magnetic field; the strength of the magnetic field is proportional to the amount of electric current. Therefore by controlling the amount of current, the magnetic field

of the electromagnets can be modified.
In order to reach the very high magnetic fields, around 8 tesla, tens of thousendds of amperes running throught the cables are required. To avoid resistive thermal load, superconductors are used, materials that lose their resistance to electric current when they are cooled enough.
So the purpose of the superconducting magnets in the LHC is to introduce magnetic fields that are necessary in order to keep the beams stable and precisely aligned, without them the particle's momentum would carry them in a straight line.
In total there are 1232 dipole magnets, which bend the beams in the circular path and also 392 quadrupole magnets, which keep the beams focalized all around the ring. In addition, there are special quadrupoles to "squeeze" the beam size, either vertically or horizontally, at the interaction points (IP) to increase the probability of collisions. Sextupole, octuple and decapole magnets are also installed in order to correct small imperfections in the magnetic field at the extremities of the dipoles.

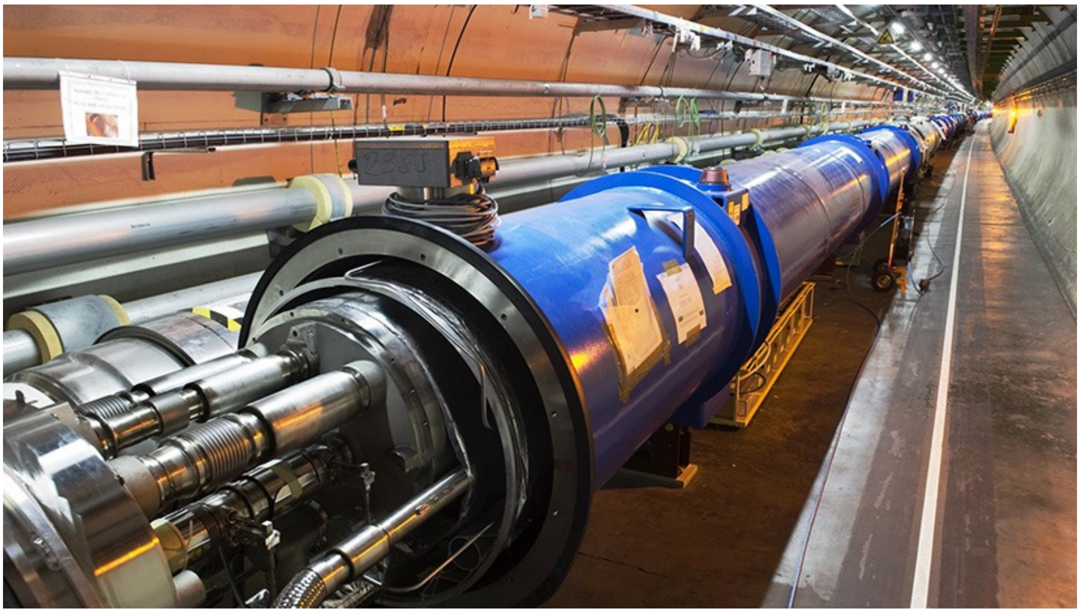

FIGURE 1.2: Superconducting Magnets in the LHC tunnel.

1.2 Standard LHC cycle

The operation of the LHC follows well-established stages, called operational modes, which together form a machine cycle.
The first phase of the LHC nominal cycle is the *"injection"*. It is divided into two distinct phases: the setup of the machine with pilot beam intensity, and the setup and injection of the physics beam. The pilot phase represents the beginning of the filling, during which a so-called pilot bunch (1×10^{10} protons) is injected into the LHC ring to guarantee the correct functioning of the magnet system. During the physics phase the LHC receives two beams from the Super Proton Synchrotron (SPS) at an energy of 450 GeV per beam. These beams arrive in bunch trains, which may consist of 1-144 bunches (1.15×10^{11} protons per bunch).
Then, both beams are ramped up (*"ramp"*) until the desired energy is reached. During this phase particles are accelerated with an electromagnetic field in the RF cavities and the magnets are synchronized in order to increase the magnetic field as the

energy.
At *"flat top"* (6.5 TeV), the machine operators initiate the beam *"squeeze"* procedure, in which quadrupole magnets are used to shrink the beam size at the experimental insertion points (IPs) to achieve the desired beam size.
The squeeze is followed by the mode *"adjust"* where the beams are brought into collision. The experiments start collecting data as soon as the mode *"stable beams"* is declared.
If equipment failures, beam instabilities or operator mistakes don't occur, the beam stays in the machine until the beam intenisty has droped enough that is better to inject a fresh beam. When this happens, the beams are aborted by the dump system located in IR6 and the machine is *"ramped down"* to injection energy in preparation for the next fill.

1.3 The LHC collimation system

The superconducting magnets, introduced above, are very sensitive to heat released by particle losses. When the energy deposition reaches a limit of 5 mW/cm^3, the magnet will loose its superconductivity (*quench*) [Burkart, 2009]. In this case, the stored energy of the magnet is dissipated as heat and the beams are dumped.
The beam stored energy of recent and future particle accelerators is shown in Figure 1.3, which includes the design (362 MJ) and achieved (150 MJ) values of the CERN Large Hadron Collider (LHC), as well as the 700 MJ goal for its high-luminosity upgrade (HL-LHC) [Redaelli, 2014].

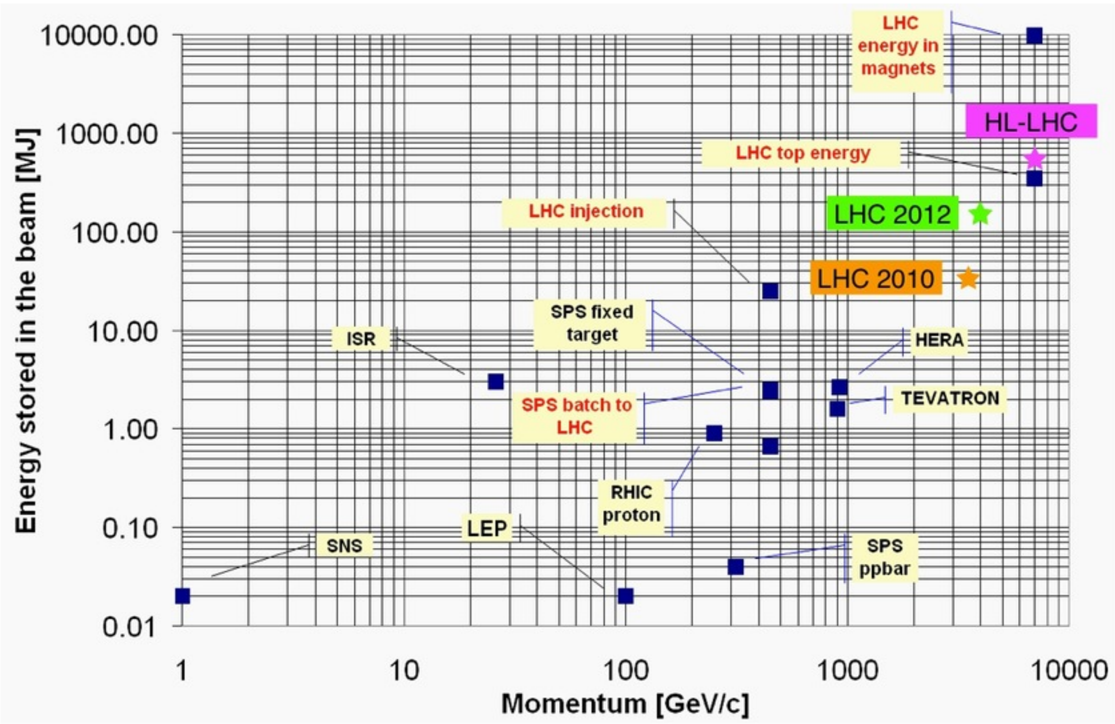

FIGURE 1.3: Livingston-like plot of beam stored energy achieved and planned for different present and future particle accelerators. Courtesy of J. Wenninger.

The quench limit of the magnets is about 10 orders of magnitude lower than the stored energy. So, to avoid them, a powerfull collimation system against beam induced losses is needed.

Collimators in proton machines were historically used to reduce the radiation back-ground at the experiments. Nevertheless, the main role of beam collimation system in the modern accelerator particles has become increasingly important in the quest for higher beam energies and intensities. The general scope of the collimation system is to dispose, safely and in a controlled way, of beam losses that would otherwise occur at sensitive locations or on accelerator equipment that is not designed to withstand beam losses.
In particular in the LHC, due to the high intensities ($I_{nom} = 3 \times 10^{14}\ p$) and the high energy ($E_{nom} = 7\ TeV$), combined with the application of superconducting magnets, a sophisticated collimation system is required, since even a local beam loss of a tiny fraction of the full beam (10^{-3} of the total beam) [Bracco, 2009] in a superconducting magnet could cause a quench, and large beam losses could cause damage to accelerator components. For this reason two machine insertions are necessary for the beam cleaning: momentum cleaning IR3 and betatron cleaning IR7.

The LHC collimation has to handle [Bruning et al., 2004]:

- *Efficient cleaning of the beam halo* during the full LHC beam cycle, such that quenches of the superconducting magnets, caused by unavoidable particle losses, are avoided
- *Minimization of collimation-related background* at the experiments to ensure clean data acquisition
- *Passive machine protection*, to protect the machine against regular and irregular losses induced by equipment failures or wrong operation of the machine.
- *Beam halo scraping and halo diagnostics*: collimator scans in association with the very sensitive LHC beam loss monitoring system proved to be a powerful way to probe the population of beam tails, which were otherwise too small compared to the beam core to be measured by conventional emittance measurements

1.3.1 Collimation System Layout

A collimator is a device that narrows a beam of particles or waves, which means either to cause the directions of motion to become more aligned in a specific direction, or to cause the spatial cross section of the beam to become smaller.
Most collimators consist of two movable blocks referred to as 'jaws' (Figure 1.4), typically placed symmetrically around the circulating beams, as far as possible from superconducting magnets.

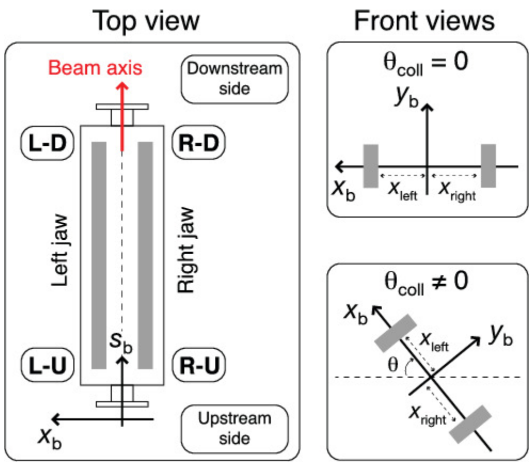

FIGURE 1.4: Top and front views of a collimator, with labels and naming conventions. Each jaw has two motors that move the jaws in the collimation plane: horizontal, vertical or skew planes. D: down-stream; L: left; R: right; U: upstream.

Four stepping motors, one at each end of the jaws, are used for aperture and angular adjustments and move the jaws with a maximum speed of 2 mm/s and a minimal stepsize of 5 μm [Bruning et al., 2004].

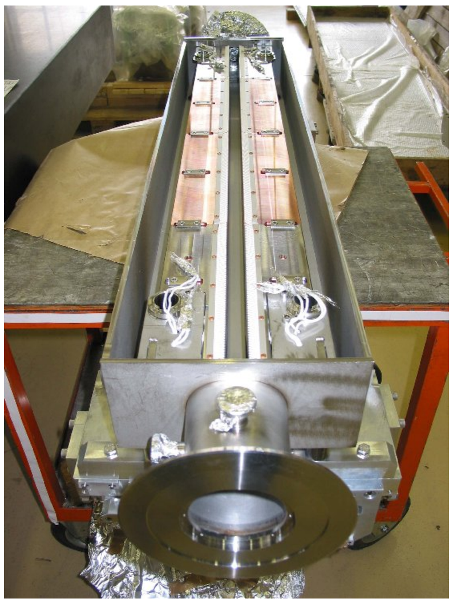

FIGURE 1.5: Horizontal LHC collimators with open tank, showing movable jaws.

A simple collimation system could be built by placing a primary collimator (TCP) in order to intercepts beam losses. This would work if the TCP were a black absorber that could stop all the primary particles at their first passage through the jaw. But the *single-stage collimation system* doesn't provide sufficiently efficient cleaning of particles populating the *halo* of the beam distribution due to various beam dynamics processes. Indeed, the halo protons that are out-scattered before being absorbed by the jaw material leave the collimator and populate the so-called secondary beam halo, which risks being lost in the machine before interacting again with the collimator in

subsequent turns.
For optimal performace, a *multi-stage collimation system* is needed (Figure 1.6), which requires additional collimators downstream of the TCP to catch the secondary halo particles. These are called secondary collimators (TCGS) and are typically longer than TCPs, to maximize the absorption of particles out-scattered at the TCPs. The TCGS aperture must be larger than that of the TCP, to ensure that the collimation hierarchy is respected without the risk of a TCGS becoming closer to the beam than the TCP, which would result in a single-stage system similar to the one discussed earlier. On the other hand, the TCGS aperture should be small enough to maximize its efficiency in catching the particles out-scattered. The TCPs and TCGSs, which are the closest collimators to the beam and hence intercept large beam losses, are made of a carbon fibre composite (CFC) to ensure high robustness since it's designed to withstand beam impacts without significant permanent damage for the worst failure cases, such as impacts of a full injection batch of $288 \times 1.15 \times 10^{11}$ protons at 450 GeV and of up to $8 \times 1.15 \times 10^{11}$ protons at 7 TeV [Appleby et al., 2017]. In addition to TCPs and TCGSs, tertiary collimators (TCLA) in front of critical bottlenecks, shower absorbers in the warm cleaning inserts, and protection devices in the dump region, are necessary to shield the machine in case of dump kicker failures. The TCLAs are made of a tungsten alloy, in order to stop as much as possible of the incoming energy. They can be less robust, in term of resistance to impact of the beam, than primary and secondary collimators because they are less exposed to beam losses.

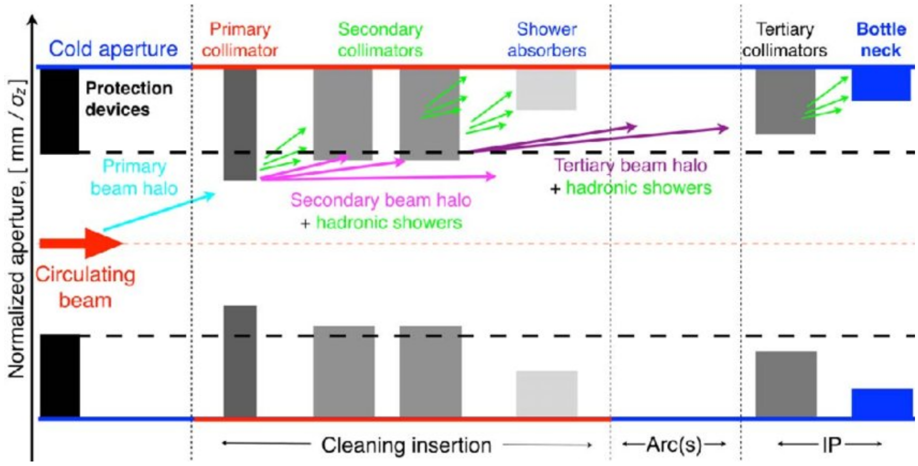

FIGURE 1.6: Schematic illustration of multi-stage collimation cleaning at the LHC.

In the LHC, the multi-stage collimation system consists of 88 collimators which are installed along the ring (44 per beam), plus 14 collimators in the transfer lines. Figure 1.6 shows a scheme of the ring collimator distribution. The main devices are primary (TCP), secondary (TCSG) and absorbing (TCLA) collimators. They are located in the two dedicated cleaning insertions in the LHC ring: the momentum cleaning in IR3 and the betatron cleaning insertion in IR7. The remaining ring collimators protect the most sensitive parts of the machine like injection (TCLI and TDI installed in IR2 for Beam 1 and IR8 for Beam 2) and extraction regions (TCDQA plus a TCSG in IR6). In addition, tertiary collimators (TCT) are installed upstream of the interaction regions to protect the triplet magnets. Absorbers (TCL) are located downstream of the IPs to catch debris from physics collisions coming from the experiments.

TABLE 1.1: Overview on the different types of collimators used in the LHC ring collimation system for both beams (H = horizontal, V = vertial, S = skew)

Purpose	**Acronym**	**Location**	**Plane**	**Number**
Primary collimators	TCP	IR3	H	2
Secondary collimators	TCGS	IR3	H	8
Absorber	TCLA	IR3	H, V	8
Primary collimators	TCP	IR7	H, V, S	6
Secondary collimators	TCGS	IR7	H, V, S	22
Absorber	TCLA	IR7	H, V, S	10
Tertiary	TCT	IR1/IR2/IR5/IR8	H, V	16
Injection protection	TDI	IR2/IR8	V	2
	TCLI	IR2/IR8	V	4
Dump protection	TCDQ	IR6	H	2
	TCSP	IR6	H	2

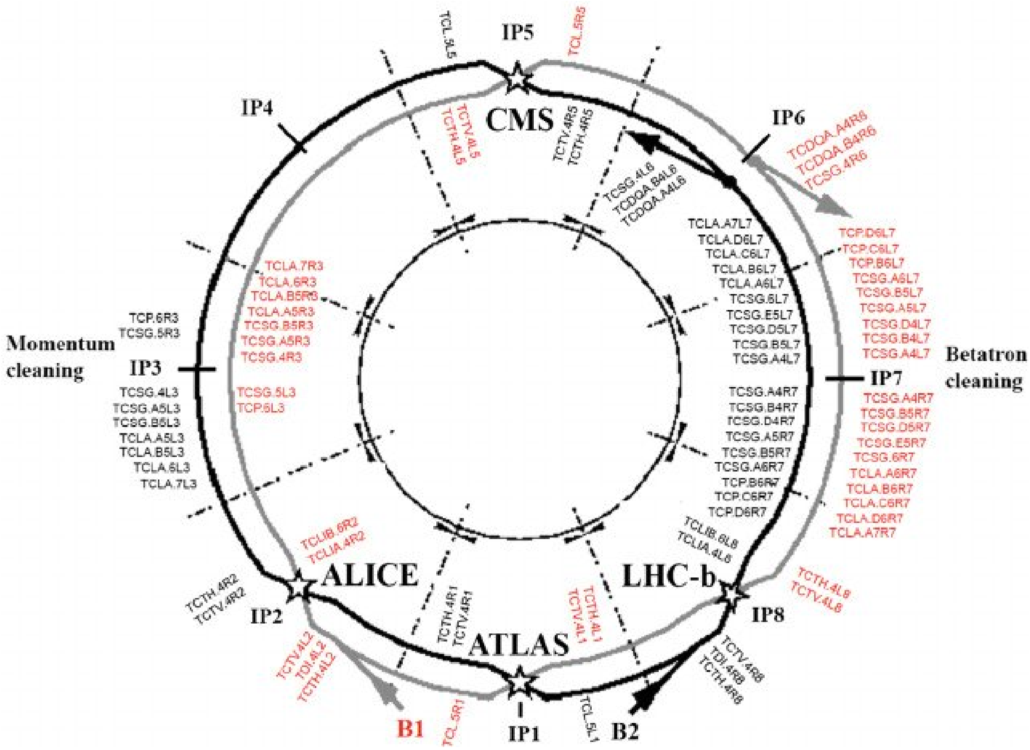

FIGURE 1.7: Collimators position in the LHC ring. Collimators are located mainly in IR3 and IR7 (on the left and right of the illustration), but also protect the experiments, the beam dump, and the transfer line regions.

Therefore, from what has been explained, highly efficient performance of the LHC collimiation system is required to safely intercept and absorb losses ans protect the accelerator from avoidable quenches.

Chapter 2

Definitions and Theoretical Background on Beam Losses

In this section is presented an overview of linear beam dynamic in storage rings, which is essential to describe the motion of a charged particles in the LHC. From this study, the main parameters, useful to define the beam profile features, are extracted. In addition, the basic concepts related to the shape of the beam in the transverse plane and the mathematical models already analyzed in previous studies and the ones on which this study is going to be carried on, are presented.

2.1 Coordinate system

In order to describe the particle motion, it is useful to introduce the cartesian coordinate system to which we will refer.
With the word *beam* we refer to the collection of a number of particles which move in a well defined direction. In the ideal machine, particles move around the *reference orbit*, which is the orbit that passes through the centre of the focusing elements of the machine. This average direction of motion is used to define the *longitudinal axis* and is indicated as s in Figure 2.1.

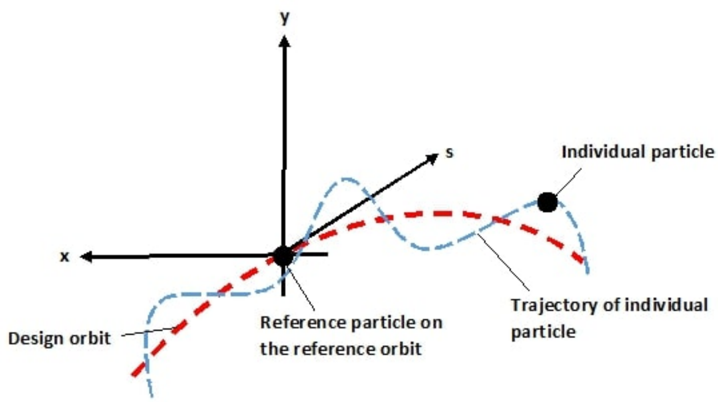

FIGURE 2.1: Trajectory of particles in the accelerator

If now we define a plane orthogonal to it, called *transverse plane*, we can identify on it the other two axes: one orthogonal to the plane containing the reference orbit, the so-called y or *vertical axis*, which usually points upward; the other one orthogonal to the two others and forming with them a right-handed reference system, this is the x or *horizontal axis*. If every time a particle crosses a transverse plane we take note of the x and y coordinates of the particle and then we transfer these points onto a

2D chart, we obtain the particle distribution in the *xy space* as shown in Figure 2.2. If there is no coupling between the motion of the particles in the x and in the y direction this distribution will be somehow elliptical with the axes of the ellipse parallel to the x and y axes.

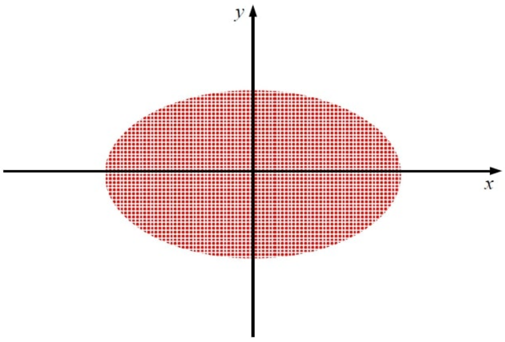

FIGURE 2.2: Particle distribution in the transverse xy space

We have also to take into account that each particle of the beam moves in a slightly different direction from the others, along the ideal orbit, thanks to focusing elements. The velocity vector components of each particle can be decomposed with respect to a 3D system (x, y, s) (Figure 2.3).

FIGURE 2.3: Decomposition of the velocity vectors into longituinal and transverse components

Assume now that we have a transverse plane and when a particle crosses it we note not only the x and y positions, but also the transverse component of the velocities, v_x and v_y. If we plot on a 2D chart, for each particle, a point corresponding to the x position and the particle's momentum x', and on another chart we do the same for the y components, we obtain the *phase space* distribution shown in Figure 2.4, which is based on the concept of velocity. The particle distributions in the phase space are again of elliptical shape, but this time the ellipses can be tilted.

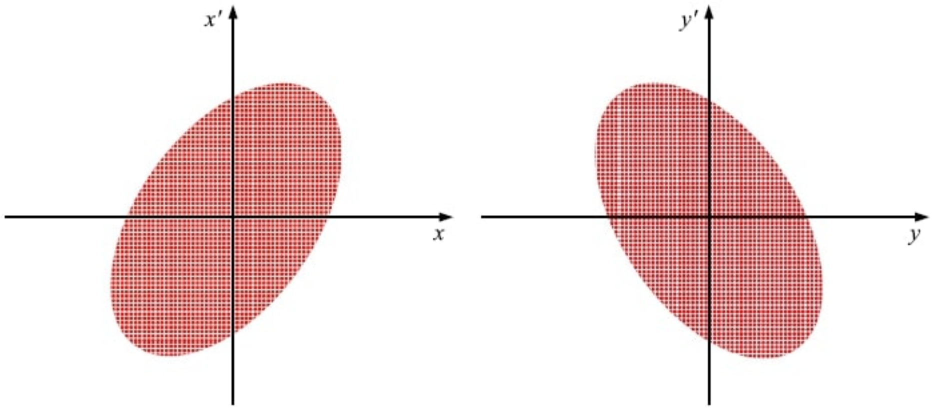

FIGURE 2.4: Particle distribution in the transverse phase spaces

In a machine where there is no coupling between the x and y planes the two phase space distributions are completely independent.

2.2 Beam Dynamics

Let's consider a beam circulating in the circular accelerator. The reference particle is the one for which $x = 0$ and $y = 0$ for all s. However in practice, it's not possible to keep all the particles on the same trajectory, indeed, the beam is populated by a number of particles performing small amplitude oscillations around the reference orbit (Figure 2.1). These oscillations are known as *Betatron Oscillation*.
For this reason, magnetic elements are choosen with the aim of guiding the beam particles along the reference path, as explained above. This is achieved by applying electromagnetic forces to the charged particles, which are intended to accelerate, bend and direct the particles on the design trajectory, or to hold them close to it.

2.2.1 Equation of Motion

The forces, which determine the motion of a particle, with a charge e, in an electromagnetic field, is described by the Lorentz law:

$$\frac{d\vec{p}}{dt} = e(\vec{E} + \vec{v} \times \vec{B}) \tag{2.1}$$

where $\vec{E}$ and $\vec{B}$ are respectively the electric and magnetic fields and $\vec{v}$ the particle velocity.
The equation of motion derives from Lorentz law and reads (Cheymol, 2011):

$$\frac{d\vec{p}}{dt} = e\vec{v} \times \vec{B} \tag{2.2}$$

Developing the vector product (Roncarolo, 2005), leads to the expression of the motion in the two transverse direction:

$$x''(s) + K(s)x(s) = 0 \tag{2.3}$$

$$y''(s) + K(s)y(s) = 0 \tag{2.4}$$

in which for the horizontal plane, the parameter K combines the focusing strength k of the quadrupole and the weak focusing term $1/\rho^2$ of the dipole field, $K(s) = 1/\rho^2(s) + k(s)$, while for the vertical plane, $K(s) = -k(s)$ (Cheymol, 2011).
These homogeneous differential equation rapresents the motion of the particles in the transverse plane and are known as *Hill's equations*.

2.2.2 Solution of Hill's Equations

The function $x(s)$ in equation 2.3 defines the transverse motion around the design orbit (betatron oscillation), $x''(s)$ denotes its second derivative with respect to the longitudinal coordinate s in the accelerator and $k(s)$ is a periodic function that is defined by the accelerator's magnet lattice.
The general solution can be found with the ansatz:

$$x(s) = a \cdot q(s) cos(\phi(s) + \phi_0) \tag{2.5}$$

where a and ϕ_0 (initial phase of the particle) are constants determined by initial conditions and $q(s)$ is a periodic function given by focusing properties of the lattice (i.e. quadupoles). The amplitude of the oscillation is given by $aq(s)$. We define the *beta function* as:

$$q(s) \equiv \sqrt{\beta(s)} \tag{2.6}$$

It represents the amplitude modulation due to the changing focusing strength. β has units of length. Of particular significance is the value of the amplitude function at the IP, β^*.
The solution to Hill's equation $x(s)$ and its derivative $x'(s)$ with respect to s, as well as the phase $\phi(s)$, can be written:

$$x(s) = a\sqrt{\beta(s)} cos(\phi(s) + \phi_0) \tag{2.7}$$

$$x'(s) = -\frac{a}{\sqrt{\beta(s)}}(\alpha(s) cos(\phi(s) + \phi_0) + sin(\phi(s) + \phi_0)) \tag{2.8}$$

$$\phi(s) = \int_0^s \frac{d\lambda}{\beta(\lambda)} \tag{2.9}$$

From equation 2.9, we can see how the rate of change of phase $\phi(s)$ of the betatron oscillation around ring is proportional to the inverse of the particle's oscillation amplitude.
The α-function is defined like:

$$\alpha(s) \equiv -\frac{1}{2}\frac{d\beta(s)}{d\beta} \tag{2.10}$$

The derivative $\beta'(s)$ is taken with respect to s. The functions $\alpha(s)$, $\beta(s)$ and ϕ are called *optical parameters*, and they only depend on the lattice properties of the accelerator.
We can define a third function that relates α and β by:

$$\gamma(s) = \frac{1 + \alpha^2(s)}{\beta(s)} \tag{2.11}$$

The parameters α, β and γ are known as *Twiss parameters* and are used for describing the linear uncoupled motion.

2.2.3 Transverse Beam Emittance and Beam Size

The solution of the linear equation 2.5, has the invariant of motion of a single particle in phase space, known as *Courant-Snyder invariant*:

$$\gamma x^2 + 2\alpha x x' + \beta x'^2 = a^2 = costant \tag{2.12}$$

in which all the variables $x, x', \alpha, \beta, \gamma$ and ϕ are function of s.
The equation $\gamma x^2 + 2\alpha x x' + \beta x'^2$ describes an ellipse in the phase space, as shown in Figure **??**. The quantity a^2 is referred as the *emittance of a single particle* following its individual trajectory. It defines the area of phase space contained by the ellipse.

$$\epsilon = a^2 = \frac{ellipse\ \ area}{\pi} \tag{2.13}$$

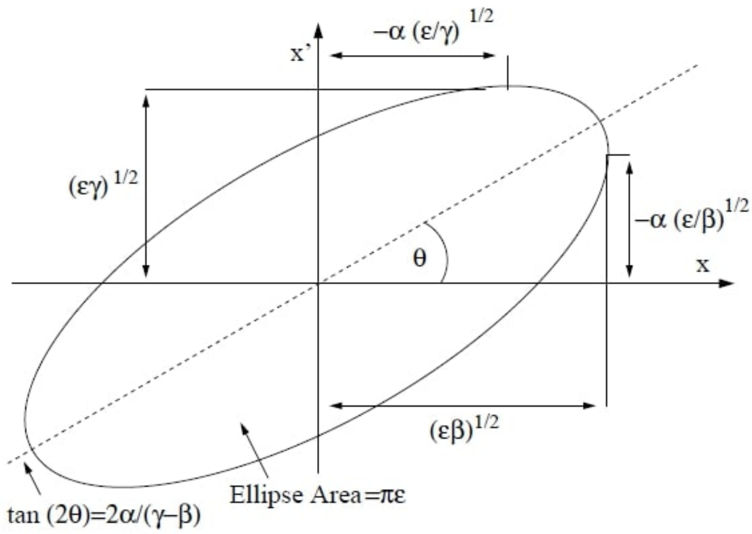

FIGURE 2.5: Ellipse mapped in the phase space relative to one transverse degree of freedom by the motion of a single particle, at a longitudinal location s

The parameters of the ellipse are determined by the lattice functions α, β and γ at the location s, and by the emittance ϵ, as depicted in Figure **??**. The ellipse in phase space may assume different orientations in different locations around the ring, but the ellipse area (i.e. the particle emittance) remains constant if the energy of the particle is kept constant and stochastic effects are neglected. This is a consequence of Liouville's theorem.
The emittance changes as a function of the beam momentum; increasing the energy of the beam reduces the emittance. It is possible, however, to construct a *normalized emittance* ϵ_r, which is invariant with the beam energy. This is defined in equation 2.14, where $\beta_{rel} = v/c$ and $\gamma_{rel} = 1/\sqrt{1 - \frac{v^2}{c^2}}$ are the relativistic beta and gamma functions, and v is the particle's speed.

$$\epsilon_r = (\beta_{rel}\gamma_{rel})\epsilon \tag{2.14}$$

Combining the concepts of emittance with the Twiss paramters, it's possibile to define the *beam size* (Roncarolo, 2005), which represents the value of the transverse particle distribution:

$$\sigma_x = \sqrt{\beta\epsilon} \tag{2.15}$$

Note that, if we assume a Gaussian distribution for the beam shape, the standard deviation of the distribution coincides with the Gaussian width σ.
From equation 2.15 it's possibile to express the emittance as:

$$\epsilon = \frac{\sigma_x^2}{\beta} \tag{2.16}$$

where σ_x is kown as *beam size* and it rapresents the value of the transverse particle distribution.
For a beam of particles, there is a whole family of similar ellipses, centered around the origin. Different particles may have differing single particle emittances, and therefore will undergo betatron oscillations of differing amplitude. A *beam emittance* may also be defined: definitions vary, however typically it is defined as the emittance corresponding to an amplitude at 1 σ of the usually assumed Gaussian charge distribution shown in Figure 2.6 (Maclean, 2014).
In a colliding beam accelerator, keeping the emittance small means that the likelihood of particle interactions will be greater resulting in higher luminosity (L). The *luminosity* is one of the most important parameters of an accelerator, it is a measurement of the number of collisions that can be produced in a detector per cm^2 and per second. The bigger is the value of L, the bigger is the number of collisions. The luminosity can be expressed as:

$$L = \frac{fN^2}{4\pi\sigma^2} \tag{2.17}$$

from which we can see that it dependes on: the number of protons N^2 because each particle in a bunch might collide with anyone from the bunch approaching head on; the bunches crossing frecuency f; the section effective of collision that depends on the cross section of the bunch, $S_{eff} = 4\pi\sigma^2$.
Assuming that vertical and horizontal β and emittances are the same, the luminosity can alsobe expressed in terms of emittances and amplitude functions as:

$$L = \frac{fN^2}{4\epsilon\beta^*} \tag{2.18}$$

Ideally $\beta*$ should be ad small as possible in order to increase the number of collisions, obviously how much small depends on the capability of the hardware to make a near-focus at the IP.

2.3 Beam Profile

Typically, as mentionated above, beam distributons are assumed to follow Gaussian distribution function, which if we consider both planes separately, is given by:

$$f(x) = \frac{I}{\sqrt{2\pi\sigma_x^2}} e^{-\frac{(x-\mu)^2}{2\sigma_x^2}} \tag{2.19}$$

$$f(y) = \frac{I}{\sqrt{2\pi\sigma_y^2}} e^{-\frac{(y-\mu)^2}{2\sigma_y^2}} \tag{2.20}$$

With reference to this shape of the profile, we can distinguish particles distributed in a *beam core* and particles in the surrounding area, called *beam halo* or *beam tail* (Figure 2.6). The latter ones are generally constituted by particles with transverse amplitudes or energy deviations significantly larger than those of the reference particle.

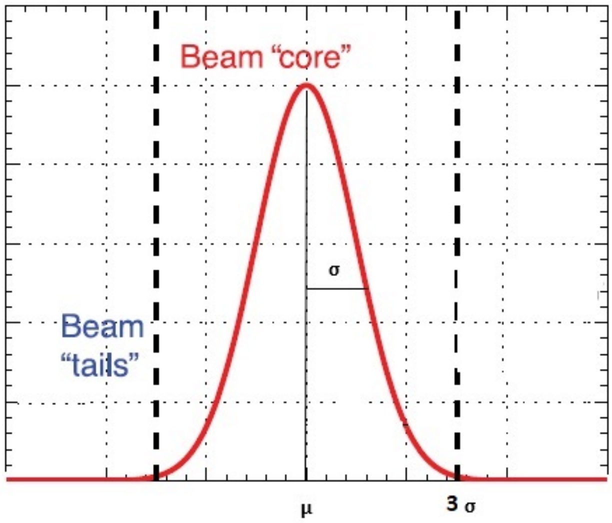

FIGURE 2.6: Standard normal distribution

The distinction between tail and core particles is, to a certain extent, arbitrary. For Gaussian distributions, one may define as halo particles those with amplitudes above 3σ (Redaelli, 2014).
Different physical processes drive particles to populate the beam halo. They are unavoidable and make cleaning necessary to minimize their effect on the elements of the machine. Some of these processes are listed below (Burkart, 2009):

- Intra-Beam scattering, causes the coupling of horizontal, vertical and longitudinal emittances due to continuous exchange of energy between the interacting particles. This leads to the increase of beam size in one dimension, which is compensated by a decrease in the other two dimensions.
- Synchrotron radiation, is the electromagnetic radiation emitted by ultrarelativistic particles when bent by electromagnetic fields. The synchrotron radiation is emitted forward tangentially to the particle trajectory taking away a fraction of the particle energy.
- Beam-Beam interaction, appens when two charged beams collide elastically scattered particles may populate the beam halo resulting in a transversal emittance growth.

Although Gaussian distributions are usually assumed, beam based tests in 2010/11 showed that the transverse particle distribution in the LHC has highly overpopulated tails, which contain up to 4% of the beam beyond 4σ (Burkart, 2009), with respect to a standard Gaussian distribution. For that reason it was concluded that the single Gaussian model does not fit faithfully the beam profile.
There are other models that take into account highly populated tails more accurately then a simple Gaussian distribution:

- *Double gaussian*, the idea behind this model is to use the sum of two single gaussian, that respectively fit the beam core and the beam tails. It was already used in prevoius analysis, like Burkart, 2009.
  The distribution (Figure 2.7) is defined as:

$$f(x) = \frac{I_1}{\sqrt{2\pi\sigma_1^2}} e^{-\frac{(x-\mu_1)^2}{2\sigma_1^2}} + \frac{I_2}{\sqrt{2\pi\sigma_2^2}} e^{-\frac{(x-\mu_2)^2}{2\sigma_2^2}} \tag{2.21}$$

  The formula shown contains some parameters which can be considered as the free parameters to adjust the fit. It turns out to be a model with six paramters of freedom, but it can be turn in a model with four parameters of freedom, if we assume the distribution centered around zero, so both μ are equal to zero. Indeed, the parameters I_1 and I_2 represent the intensity of the two single gaussians and σ_1 and σ_2 are the respective variances, which correspond to the beam size, since the gaussian distirbution is assumed.

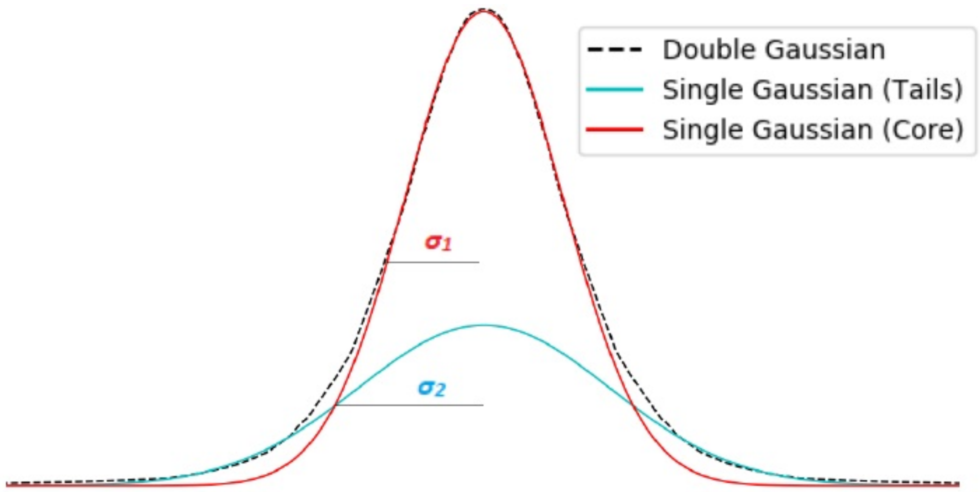

FIGURE 2.7: Double Gaussian distribution

  Moreover, it's possibile to move form a model with four parmaters of freedom to a three parameters of freedom one, if we take into account, with reference to Fiugre 2.7, that in $x = 0$ the sum of the intensites is equal to the integral of the distribution.

- *Lévy Student*, it is taken into account since it has got hevier tails then the Gaussian distribution:

$$f(x) = \frac{\Gamma(\frac{n+1}{2})}{\Gamma(\frac{1}{2})\Gamma(\frac{n}{2})} \frac{a^n}{(x^2 + a^2)^{(\frac{n+1}{2})}} \tag{2.22}$$

where a plays just the role of a scale parameter, while n rules the power decay of the tails.

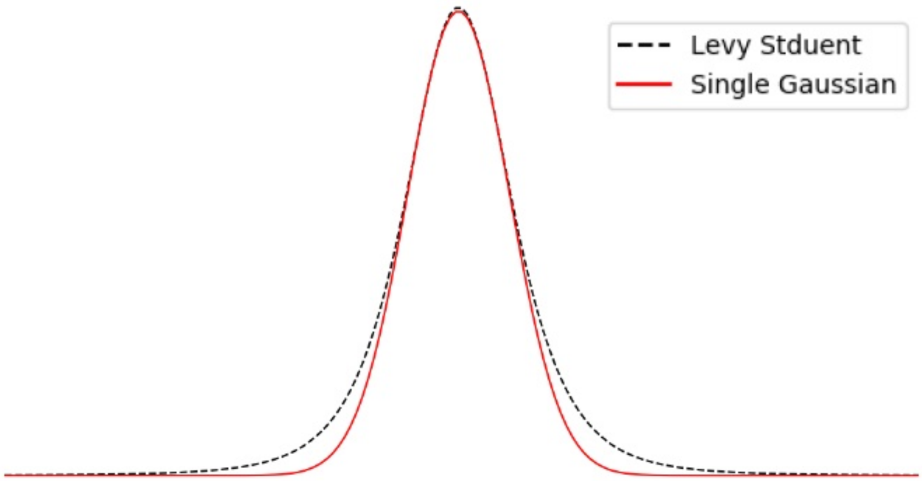

FIGURE 2.8: Lèvy Student distribution

The Student law should not be radically different from a Gaussian: in fact the halo is in some sense an effect that is small when compared with the total beam. From this standpoint the family of studnet laws has also the advantage that we can fine-tune the parameters n, a in order to get the right distance from the Gaussian laws (Martino, Siena, and Illuminati, 2005). With this hypothesis in mind, in this work we will limit our considerations to the case n real quantity greater than 2 in order to have a finite sigma and under these conditions $a^2 = (n-2)\sigma^2$ (Giovannozzi, 2012).

To improve the agreement between the beam profile and the model used to fit it, these two models are taken as the baseline reference for the analysis carried out in the following chapters, since their distribution can potentially follow in a better way the shape of the beam tails.

Chapter 3

Beam Instrumentation for Profile Reconstruction

All beam instrumentations for high-intensity hadron beams are characterized by an important feature, which is the required *dynamic range*. Typically the instrument has to cover signals coming from low-intensity beams during commissioning up to very-high-intensity beams after an upgrade of the accelerator. “Pilot bunches”, with $10^{10}p$, have to be diagnosed to ensure that the whole accelerator chain has been set up correctly before injecting the full beam. Often the beam has a large diameter, especially non-relativistic beams. Therefore, large size beam monitors with large apertures are needed.
An other important feature of high-intensity beam instruments is that some diagnostic systems have to create a beam interlock or allow the signal to protect the machine against damage from unmatched beams. Therefore, their high reliability and availability as well as their accurate and stable work are necessary to ensure high productivity of the accelerator.
The following sections summarize the most important instruments for sufficient beam diagnostics of high-intensity hadron beams: beam loss monitors, current transofrmers, profile monitors (Wittenburg, 2013).

3.1 Beam Loss Monitor

The loss of a very small fraction of the circulating beam may induce a quench of the superconducting magnets or even physical damage to machine components. Therefore, a system to protect the machine equipments against unintended energy deposition by losses is necessary.

To achive this goal the *Beam Loss Monitor (BLM) System* is installed all around the ring (Figure 3.1). Its main purpose is to convert particle shower information into electrical signals, which are then compared with thresholds. If these are exceeded, extraction of the LHC beam from the ring is initiated to stop the irradiation of equipment. The treshold levels for beam extraction are lower (orders of magnitude) than for the damage protection of equipment in order to protect the machine against serious damage. In addition to the protective functionality, the loss detection allows the observation of local aperture restrictions, orbit distortion, beam oscillations and particle diffusion, etc. Since a repair of a superconducting magnet would cause a down time of several weeks, the protection against damage has highest priority.

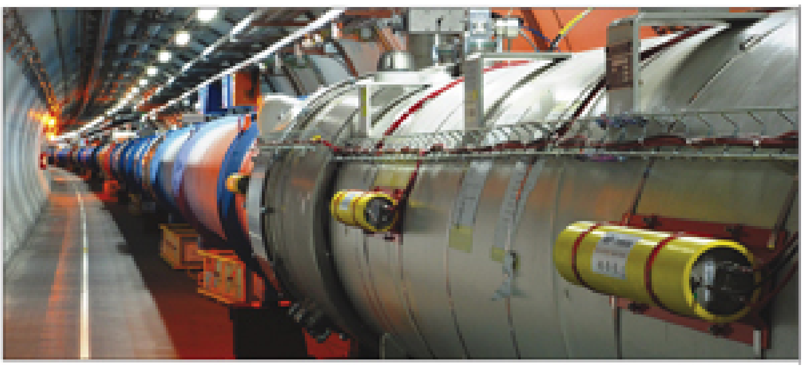

FIGURE 3.1: Beam Loss Monitor installed along the LHC ring

3.1.1 Ionization chambers

The measurement principle is based on the energy deposition detection of secondary shower particles using *ionization chambers*. An ionization chamber in its simplest form consists of two parallel metallic electrodes (anode and cathode) separated by a gap of width D of $5\mu m$ and an applied bias voltage of a $1500V$ (Bruning et al., 2004. The gap is filled with N_2. The gas-filled volume between the electrodes defines the sensitive volume of the chamber. Ionizing radiation creates electron–ion pairs in this sensitive volume. The electric field $E = \frac{V}{D}$ causes electrons and positive ions to drift in opposite directions toward the anode and cathode, respectively. The number of electrons reaching the anode depends on the applied voltage. If the voltage is very small, the electrons produced by ionization recombine with their parent ion. The electrons can escape this immediate recombination if the electric field between the electrodes is larger than the Coulomb field in the vicinity of the parent ion. The number of electrons collected at the anode increases with voltage up to saturation where all charges are collected. In this ionization region the created charge should not depend on the applied voltage. At higher voltages, the electrons gain enough energy to produce ionization on their path.
Therefore, a high voltage and a small gap D are preferred to achieve a high dynamic range as well as to achieve a faster response time of the ionization chamber.

3.1.2 Positioning of BLMs

BLMs should be localized in areas with higher probability of beam losses. More then 1000 BLMs are installed all around the ring and each of them, at each location, needs its own specific efficiency calibration in terms of lost particle. The loss of a high-energy particle in the wall of a beam pipe results in a shower of particles which leak out of the pipe. The efficiency of a loss detector will be highest if it is located at the maximum of the shower. The length of the shower depends on the energy of the lost particle and ranges from some metres, for very high proton energies, to a few centimetres, for medium electron energies. Therefore the expected location of lost particles has to be studied in advance so as to situate the monitors at the right place. Since the quadrupoles always have a local β maximum, either in x or in y, they are the preferred locations for BLMs around an accelerator. This is especially true for BLMs which have to serve the quench protection system in superconducting accelerators (Wittenburg, 2013). Detailed Monte Carlo simulations can help find the optimum positions of BLMs at the superconducting quadrupoles as well as the efficiencies at these positions. Generally, their longitudinal positions are about $1m$ downstream of the most likely loss locations. (Bruning et al., 2004).

3.1.3 Dynamic Range and Families of BLM

The criteria used to define the *dynamic range* are given by the calculated damage and quench levels and the expected usage, and it is defined by its upper and lower current signal. The upper limit is given by the non-linearity due to the recombination rate at high dose (few hundred μA). The lower limit is given by the dark current between the two electrodes, in order to keep it at low level (few pA), a very careful design of the chamber is necessary.
Four different families of BLM monitors, listed in Table 3.1, are defined to ease the monitor design:

- BLMA, which represents the highest number of monitors installed around the quadrupole magnets all around the ring. They constitute local aperture minima, and therefore likely loss locations.
- BLMS, installed at global aperture limits other than the collimators and other critical loss locations.
- BLMC, installed after each collimator, are used to set the position of the collimator jaws and to continuously monitor their performance.
- BLMB, which will only be installed after the commissioning of the LHC, to be used for dedicated beam studies on a bunch scale.

TABLE 3.1: Families of BLM

Type	**Locations**	**Purpose**	**Dynamic Range**
BLMA	All along the rings (6 per quadrupole)	Protection of superconductiong magnets	10^8
BLMS	Critical aperture limits or critical positions	Machine protection and diagnostic of losses	10^8 or 10^{13}
BLMC	Collimation sections	Set-up the collimators and monitor their performance	10^{13}
BLMB	Primary Collimators	Beam Studies	10^8

There are basic criteria common to the BLMA, BLMS and BLMC (Bruning et al., 2004):

- The high end of the dynamic range is set at three times the quench level. This takes into account the uncertainty of the evaluation of the quench level (factor of two). It also leaves, between the dump threshold and the high end of the BLM dynamic range, a safety margin of a factor of 9 at $450GeV$ and of a factor 7.5 at $7TeV$.
- The low end will be 5% of the quench level.

3.2 Beam Current Transformer

The number of particles forming the beam, referred to as beam intensity, is one of the most fundamental operational parameters for any accelerator. The directly measured quantity is a beam current, which is then integrated during a specific time to evaluate the beam charge, expressed as the beam charge divided by the elementary charge. As the measurement monitor is sensitive to the beam current it is called *Beam Current Transformer (BCT)*.
The beam current monitors fall into the category of non-intercepting measurements. The monitors are inductively coupled to the beam providing an electrical current proportional to the beam current.
Beam current transformers provide intensity measurements for the beams circulating in the LHC rings as well as for the transfer lines from the SPS to LHC and from LHC to the dumps. The transformers are all installed in sections where the vacuum chamber is at room temperature and where the beams are separated (Bruning et al., 2004).
Particulary, two different kinds of beam current transformers provide intensity measurements for the beams circulating in the LHC rings as well as for the transfer lines from the SPS to LHC and from LHC to the dumps.

3.2.1 DC Beam Current Transformers

The *DC Beam Current Transformer (BCTDC)* measures an intensity of a circulating beam. The principle of operation is shown in Figure 3.2. The measurement device uses a "magnetic modulator" to obtain a signal proportional to the DC current of the beam. Magnetic modulation is done by superposition of the magnetic flux generated by a signal of a generator with the beam signal. The modulation flux develops from injection of a current into windings of two magnetic cores. The windings configuration is such, that the current generates in both cores a flux of opposite direction. A common sensing winding provides an output signal.

FIGURE 3.2: Priciple of operation of a DC Beam Current Transformer

Because of their operational importance, two of the devices will be installed in each ring. Currently a resolution of $2\mu A$ can be reached but a $1\mu A$ is targeted corresponding to 5×10^8 circulating particles (Bruning et al., 2004). The reaction time of the feedback loop is usually some tens of ms. Due to that, the BCTDCs can not measure on transfer lines (Belohrad, 2010).

3.2.2 Fast Beam Current Transformer

The *Fast Beam Current Transformers (FBCTs)* provides complementary measurements to the BCTDCs. The FBCTs are typically used in the transfer lines, to measure injection and extraction efficiency, or provide measurements of low energy and intensity beams. The principle of measurement is shown in Figure 3.3.
A toroidal transformer is used to measure the current. It couples inductively to the beam current. To make the transformer to "see" the beam current the vacuum chamber must be split into two parts and separated by an isolator. In order to provide a conducting path for the wall image current the toroid is bypassed from outside by a low impedance RF connection. Such configuration permits to integrate a current induced in the winding and evaluate the number of charges. The FBCTs often use two windings. The first winding, referred as a calibration turn, is used to inject a known current into the transformer. The second winding is connected to an acquisition system and provides the measurement signal.

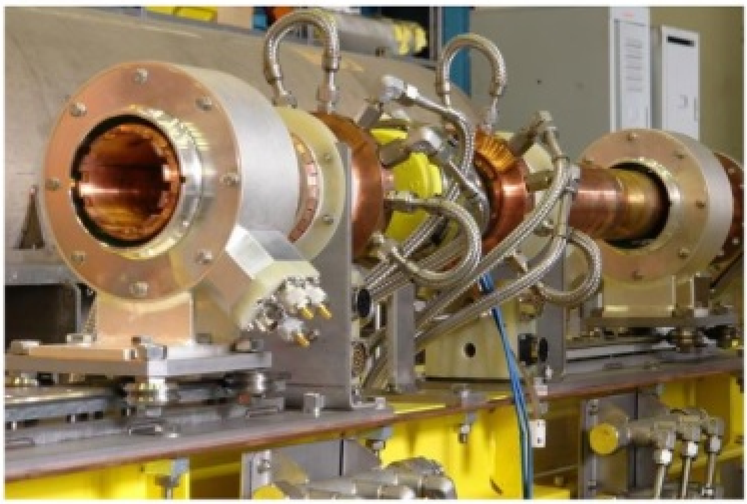

FIGURE 3.3: Principle of operation of a Fast Beam Current Transformers

FCBT provides good accuracy for both bunch to bunch measurements and average measurements, mainly for low intensity beams for which the BCTDC accuracy will be limited. For redundancy, two transformers, located in IR4, with separated acquisition chains will be placed in each ring. Each beam dump line will also be equipped with two redundant FBCTs, using the same acquisition electronics, for monitoring the ejected beam. The measurement precision for the pilot beam of 5×10^9 protons in a single bunch is expected to be around 5% (worst-case 10%), for the nominal beam below 1% (Bruning et al., 2004).

3.3 Beam Profile Monitors

Beam profile measurements are essential to get a good understanding of the beam dynamics in the machine and to minimize beam losses along the accelerator. In addition, profile monitors are indispensable to measure the emittance evolvement. The profile measurement needs to be minimally invasive for two reasons: to avoid influencing the beam and to avoid destroying the monitor.
A wire scanner is an electro-mechanical device which measures the transverse beam

profile, by means of a thin wire moving in an intermittent manner orthogonaly to the beam trajectory. The interaction of the wire and the beam generates a cascade of secondary particles, which are intercepted by a scintillator, located outside the beam pipe. Those one is coupled with a photomultiplier (PM), which measures the intensity of the light thus produced and has two basic stages: the conversion of photons into electrons and the electron multiplication intended to enhance the signal level in order to improve the signal over noise ratio. The current generated from the PM is proportional to the beam intensity at the position of the wire, combining both the informations allows the reconstruction of the transversal beam intensity profile. This profile is processed to obtain the transverse size and combined with other information to obtain the emittance of the beam. The wire scanner position is measured with a high precision potentiometer.
The *Beam Wire Scanner (BWS)* belongs to the category of interceptive beam transversal profile measurement system. In particular, it is usefull to measure bunch-by-bunch transverse beam size and emittance for each beam and plane. To achive this purpose, two sets of four wire scanners are installed in the LHC, one wire scanner for each beam and plane and in addition a sparete set of wire scanners is used as a backup in case of damages of the operational instrument.

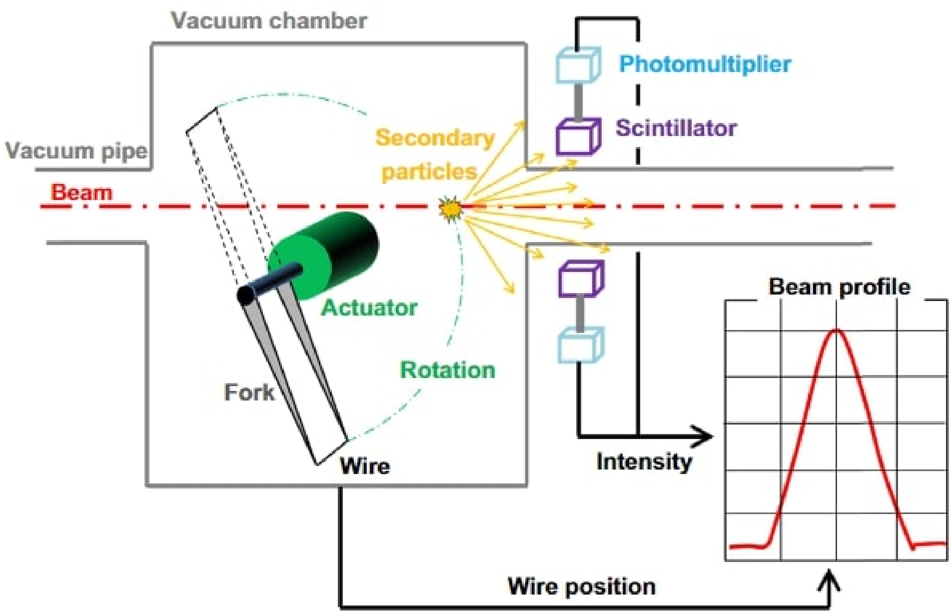

FIGURE 3.4: Schematics of the wire scanner instrument

The full wire scanner system can be divided into three subsystems: the wire, the actuator, and the control system (Herranz, Barjau, and Dehning, 2016).

- The *wire*, which is stretched by a fork directly mounted on a shaft, both located in a vacuum chamber
- The *actuator*, located outside the vacuum chamber, provides a motion pattern consisting of three distinct phases (acceleration, constant speed and deceleration) fulfilling a set of requirements in order to achieve a suitable wire speed and position at beam crossing.
- The *control system*, which includes the controller, the power amplifier and the electrical part of the actuator)

In the LHC, the wire scanners are installed in IR4 and IR5 and they are routinely operated in the "bunch mode" which gives one transverse profile for each bunch. They are equipped with a $36\mu m$ carbon wires attached to the fork, which crosses the beam at a constant speed of $1m/s$ (Kuhn, 2013), defining the precision of the measurement. Slower is the movement of the wire, more accurate is the measurement. The wire scanner passes through the beam twice per measurement: *scan in* and *scan out*. The obtained beam size is averaged over the in and the out scan. Thus, the emittance value evaluated contains the error from the fit, the error from averaging of in and out scan and the error on the beta function.
Errors on the wire position when intersecting the beam have a direct consequence on the profile and position measurement accuracy. Thus, identifying and minimizing the uncertainties and error sources is a priority issue. In 2015, measurements of the wire scanner length scale using the beam position monitors (BPM) have shown discrepancies $< 5\%$ on the beam position, which is within the uncertainty on the BPM length scale (Hostettler et al., 2017).
The precision of the wire scanner is predominantly dominated by the noise, both on the wire position and on the signal acquired from the photomultiplier. In online measurements, a scan-to-scan spread of 10% on the measured emittances has been observed. When reprocessing the wire scanner data offline, the position readings can be smoothed by applying a linear fit, while the noise on the signal can be reduced for isolated bunches by scanning and subtracting the noise in empty bunch slot just before each bunch (Hostettler et al., 2017).

Chapter 4

Collimator scraping for profile reconstruction

To evaluate the realistic particle distribution in the transverse plane of the beam one has to measure the particle density. This has been performed with collimator scrapings, mesuring the population of the beam in the horizontal, vertical and skew planes, using the primary collimators of the LHC collimation system.
Ususally primary collimators in IR7 are used for the scraping measurements, as they are the most robust collimators. Before the scraping, the collimator jaws must be aligned with respect to the beam position in order to obtain the precise location of the beam center. During a scraping one of the two collimator jaws is moved into the beam to scrape away particles. The reconstruction of the beam profile is performed taking into account the beam losses recorded in the BLMs close to the collimator used for the scraping (Figure 4.1) and the bunch intensity reduction.
It should also be considered that the scraping performed is a fast scraping, in such a way that the beam diffusion mechanisms can be neglected. In fact, in the case of slow scraping there is a process of diffusion of particles from the core that repopulate the tails.

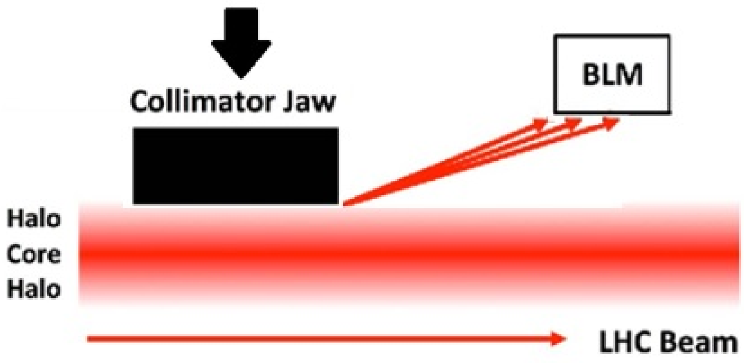

FIGURE 4.1: Collimator scraping and losses recored in the BLM close to the collimator

4.1 Calibration Factor

From the beam intensity profile during the scraping it is possible to estimate the beam population scraped at each position of the collimator. To get the instantaneous losses on a collimator it is necessary to calibrate the beam intensity signal from the FBCT to the signals from the BLM, S_{BLM}, on the corresponding collimator.

Calibration factors f^i_{calib} depend on the *running sums (RS)* of the BLM signals, which are different integration times for the BLM signals, that allow the analysis of losses with time scales from 40 μs up to 83.88 s (Burkart, 2009). Figure 4.2 shows the available BLM running sums for BLM signals published and logged with a frequency of $1Hz$.

Signal Name	Time windows		Refreshing		Data formats	
	Number of 40 µs steps	Duration [ms]	Number Of 40 µs steps	Duration [ms]	FPGA/VME	Measurement & Logging DB (rate: 1 Hz) [Gy/s]
RS01	1	0.04	1	0.04	Maximum of sum values observed from the last readout	Maximum of sums normalised to window length
RS02	2	0.08	1	0.04		
RS03	8	0.32	1	0.04		
RS04	16	0.64	1	0.04		
RS05	64	2.56	2	0.08		
RS06	256	10.24	2	0.08		
RS07	2048	81.92	64	2.56		
RS08	16384	655.36	64	2.56		
RS09	32768	1310.72	2048	81.92	Last calclulated sums observed in the last readout	Last calculated sum normalised to window length
RS10	131072	5242.88	2048	81.92		
RS11	524288	20971.52	16384	655.36		
RS12	2097152	83886.08	16384	655.36		

FIGURE 4.2: Available BLM running sums in the LHC.

In particular, the ones used for this work is $RS01$. Note that during the beam scrapings the loss is compared to the integration time. Therefore the BLM signals S_{BLM} have to be divided by the running sum to get a real signal for the particle loss, which is not diluted by the integration over a time interval. For the analyzed case we have:

$$S^{loss}_{BLM} = \frac{1}{1.3} S_{BLM} \tag{4.1}$$

4.2 Intensity Loss during Collimator Scraping

The instantaneous particle loss rate (R_i) at collimator i can be calculated with the calibration factor and the BLM signal as (Burkart et al., 2011):

$$R_i(t) = f^i_{calib} S_{BLM}(t) \tag{4.2}$$

If we consider that the jaw is moved every $4s$ and with the logging frequency of the BLM signals of $1Hz$, the *lost intensity* at each collimator jaw position u is given as:

$$I_L(u) = \sum_{j=1}^{4} (R_i(t_{u,j}) \cdot 1s) \tag{4.3}$$

where $t_{u,j}$ is the time when the collimator jaw is on position u.
The remaning intensity in the beam at each colliator jaw position u can then be written as:

$$I(u) = \sum_{u}^{u_{end}} I_L(u) = \sum_{u}^{u_{end}} \sum_{j=1}^{4} (-R_i(t_{u,j}) \cdot 1s) \tag{4.4}$$

with $I(u_{end}) = 0$.
The total intensity is given by:

$$I_{total} = \sum_{u_{start}}^{u_{end}} I_L(u) \tag{4.5}$$

where u_{start} is the starting position of the collimator jaw.
The normalized, integrated, lost intensity at the collimator jaw position u can be calculated as:

$$I_{tot,lost}(u) = \sum_{u_{start}}^{u} I_L(u)/I_{total} \tag{4.6}$$

4.3 Particle Loss during Scraping

Assuming a Gaussian distributon for the beam profile and using normalized coordinates x, x', the horizontal and vertical phase space distribution can be written as a two-dimensional Gaussian of the form (Burkhardt and Schmidt, 2004):

$$g_2(x, x') = \frac{1}{2\pi} e^{-\frac{x^2+x'^2}{2}} \tag{4.7}$$

where g_2 is normalized to 1.
Multiple passages at the scraper result in a round cut at $n_\sigma = \sqrt{x^2 + x'^2}$. The remaingin particles (Figure 4.4) are distributed according to:

$$g_r(x) = \int_{-\sqrt{n_\sigma^2 - x^2}}^{\sqrt{n_\sigma^2 - x^2}} g_2(x, x')dx' = \frac{e^{-x^2/2}}{\sqrt{2\pi}} erf(\sqrt{\frac{n_\sigma^2 - x^2}{2}}) \tag{4.8}$$

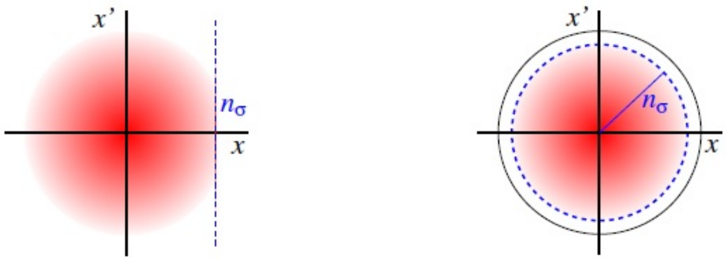

FIGURE 4.3: Single sided cut after a single passage at a scraper (left) and round cut after many passages at the scraper (right).

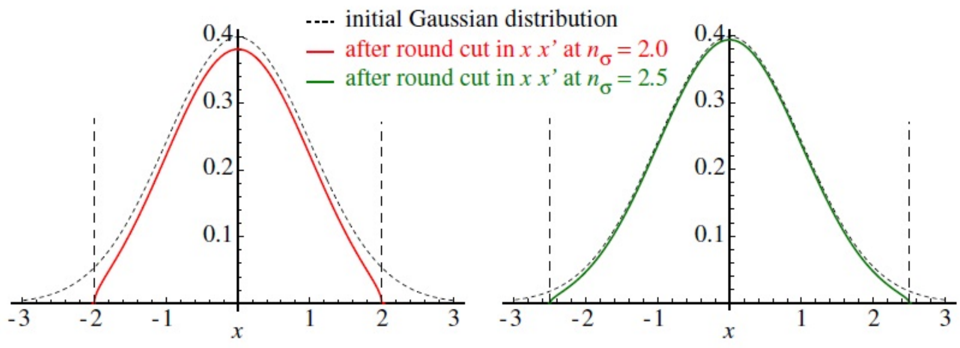

FIGURE 4.4: Gaussian beam profile before (dashed line) and after (solid line) collimation at $n_\sigma = 2.0$ (left) and $n_\sigma = 2.5 (right)$.

The fraction of remaning particles is:

$$F_r(n_\sigma) = \int_{-n_\sigma}^{n_\sigma} g_r(x)dx \tag{4.9}$$

This integral can be evaluated analytically in polar coordinates $x = rcos\phi$, $x' = rsin\phi$, $dxdx' = rdrd\phi$, $0 \leq \phi \leq 2\pi$ and $0 \leq r \leq n_\sigma$. We find, that the fraction of particles left after craping at n_σ over many turns (corrisponding to a round cut in phase space) is (Figure 4.5):

$$F_r(n_\sigma) = \frac{1}{2\pi}\int_0^{n_\sigma}\int_0^{2\pi} re^{-r^2/2}d\phi dr = \int_0^{n_\sigma} re^{-r^2/2}dr = [-e^{-r^2/2}]_0^{n_\sigma} = 1 - e^{-n_\sigma^2/2} \tag{4.10}$$

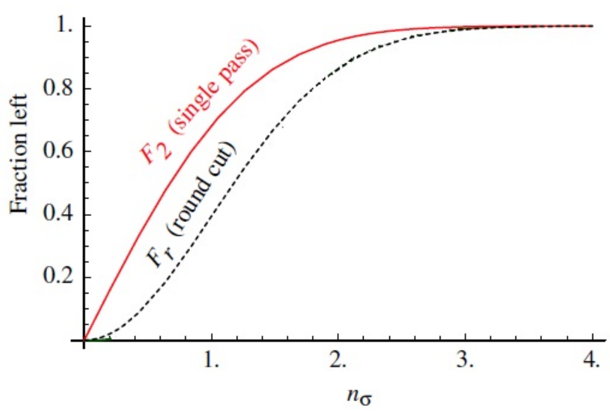

FIGURE 4.5: Fraction F_r of particles left after many passages at a scraper and fraction of particles left after a single passage through a two-sided scraper F_2.

It is clear that, while when the collimator is moved through the tails, the remaining fraction of particles is reduced slightly, as the collimator approaches the core of the beam, it tends more quickly to zero. This is due to the fact that the number of particles in the tails is much lower than those of the core.

Chapter 5

Beam Profile Modeling

A *Python script* has been developed with the aim of fitting the beam profile. The choice of the programming language is due to the fact that it already includes the tools required for the analysis.
Since the script is very structured, we decided to present it in detail in order to understand how it works.
The analysis can be mainly divided in four blocks (Figure 5.1): profile reconstruction from collimator scans, profile fitting, profile reconstruction from the BWS and comparison between the reconstructed profiles with the theoretical Gaussian.

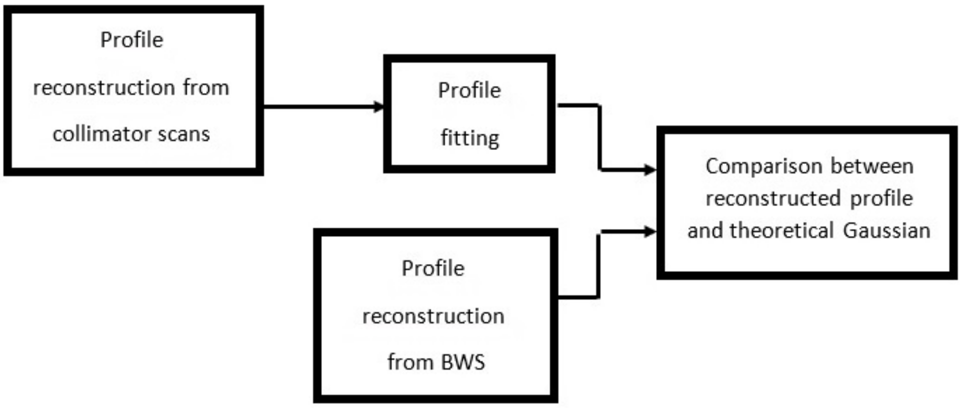

FIGURE 5.1: Diagram of the analysis for profile reconstruction

5.1 Beam Profile Reconstruction from Collimator Scans

For the reconstruction of the beam profile from the collimator scans a function has been defined with the purpose of matching the data extracted from the BLM with the collimator positions between two time instants ($t01$ and $t02$).
Through *PyTimber*, which is a Python API for querying data of the CERN Accelerator Logging Service, two arrays of numbers were obtained, for both the BLM signal and the collimator position, which respectively represent the time (tt_{BLM}) and the value (vv_{BLM}) of each acquisition in the first case and the time (tt_{TCP}) and the position (vv_{TCP}) in the second one.
The storage and fast retrieval of measurement data is essential for system checks, but also the check of noise amplitudes of the system is very important. Particle loss, natural radiation, thermal noise contribute to the BLM background. To estimate it, a time interval of 60 s was taken into consideration and the average of the signal extracted from the BLM, between these the two time instants, was calculated. It should be noted that the background to which it refers is that calculated with the beam in

the machine.
The avarage of the BLM signal over 60 seconds was choosen to be enough before some long term effects of the beam, such as emittance jumps, a shorter time, however, could induce a smaller or larger background than the real one beacuse of the signal fluctuations. The noise level, thus defined, is important because it is subtracted from the extracted values of the BLM signal, and the result is stored in a new vector, max_BLM, in order to obtain a more realistic measurement of the number of scraped particles.
Since we need to synchronize the BLM signal and the position of the collimator, the data that we want to observe are those that go from the beginning to the end of the scraping, because before and after it the collimators do not move. A function that allows to retrieve the collimator position as a function of time has been implemented and it could be find in 8.
The time in which the collimator starts moving and the one in which it stops represent the starting and finishing points of the observation window of interest. Once it has been defined, each value of the tt_BLM vector is compared with those of the tt_TCP vector in order to find the time where, for a given collimator position time interval, the BLM signal time falls in this interval. When this occurs, a match is obtained between the BLM signal, corrected by the noise level, and the collimator position.
Let's note that the BLM signal is proportional to the number of lost particles. This proportionality factor, known as the calibration factor, can be calculated by summing all the values contained in the max_BLM array and then dividing the sum (*cummulative*), which is in Gray (Gy), by the number of scraped particles, evaluated previously as the difference between the two intensity values. If now we normalize *cummulative* with respect to the calibration factor we obtain the number of protons. If the result is normalize again, with respect to the maximum value of intensity, we obtain the fraction of scraped particles at each position of the collimator. This is what we need to reconstruct the beam profile when a scraping is done.
The collimator position can be express in both *mm* or beam size units (σ). We have to take into account that collimators are not centered with respect to the zero, but they are centered with respect to the beam. Therefore, in order to find the center of the beam we need to sum the starting positions of both collimators and then dividing by two.
In this work, as previously mentioned, only one jaw was moved and the reconstructed profile was then mirrored in order to simulate the complete trend of the beam profile. Moreover, in order to be able to exploit a model for the fit with the least possible number of free parameters, the profile obtained was centered with respect to zero, that means that $\mu = 0$.

5.2 Beam Profile Fitting

Once the beam profile was reconstructed from the collimator scan, the fit was made using both the Double Gaussian model and the Lèvy Student one. The choise to use the BLM for the profile reconstruction was dictated by the greater resolution of the instrument with respect to BWS.
For what concern the curve fitting and the optimization routine used, the first idea was to use *numerical integration*. Indeed, the BLM signal needs integration because in every step what is obtained is a delta signal corresponding to the particle contained in the range of the jaw. Therefore, an integration of the distribution from an

initial to a final position of the collimators is necessary. Obviously the position of the collimators is a function of time, so the integral of the distribution can be turned into the integral between two time instants of the BLM signal $l(t)$ (measured values).

$$\int_{x_i}^{x_j} \rho(x)dx = \int_{x(t_i)}^{x(t_j)} \rho dx = C\int_{t_i}^{t_j} l(t)dt \tag{5.1}$$

with C, conversion factor from Gy to protons.
The first and last integral of equation 5.1 can be computed using a numerical integration method, which is an approximation, known as *Simpson's rule* (*Simpson's rule*). This method provides the subdivision of the integration interval into sub-intervals and the replacement in these sub-intervals of the integrand function by means of parabola arcs, that is by quadratic polynomials. It is shown that Simpson's formula is:

$$\int_a^b f(x)dx \simeq \frac{\Delta x}{3}(f(x_0) + 4f(x_1) + 2f(x_2) + ... + 4f(x_{n-1}) + f(x_n)) \tag{5.2}$$

with Δx amplitude of the sub-intervals. To do it, a function has been implemented and is shown below only for the case of Double Gaussian model.
Applying the method leads to:

$$\int_{x_i}^{x_j} \rho(x)dx = \sum_{k=i}^{j} \alpha_k \rho(x_k) \tag{5.3}$$

$$\int_{t_i}^{t_j} l(t)dt = \sum_{k=i}^{j} \beta_k l(t_k) \tag{5.4}$$

in the end, what is obtained is the equality between the two summations:

$$\sum_{k=i}^{j} \alpha_k \rho(x_k) = \sum_{k=i}^{j} \beta_k l(t_k) \tag{5.5}$$

where α_k and β_k are given by the integration method and with reference to the latter one, it includes also the conversion factor C.
Since the distribution is unkonwn a priori, that means that the values of its free parameters are unknown, the idea was to evaluate the integral of the BLM signal and compare it with the ones of the distribution defined by choosing one of the models explained before, in which the parameters were searched in order to provide the least possibile difference between the two integrals (AppendixA). For simplicity, the optimization technique chosen is the least square method (*Least Squares*). This method presented two main problems: the first one is that it is necessary to choose the intial values for the model parameters, and these must be close to the useful ones; the other one is that we should establish the necessary number of cycles through which to iterate to find the optimal values of the parameters. Unfortunatelly, this information is not known in advance.
It was, therefore, thought to make use of the *Lmfit library*, already implemented in Python, that provides a high-level interface to non-linear optimization and curve fitting problems. Starting from a function of the parameterized model, it adjusts the numerical values of the model so that it corresponds more closely to the set of data. The difference with the previous method is that this library accepts as initial parameters any value, even if not close to those sought. Indeed, it offers the advantage of

being able to define constrains for the parameters of the model distribution. This is usefull since, as explained above, there are constrains to respect for both the models. By default the optimization method used by this library is the least squares method, but there is the possibility to modify the adaptation algorithms.
The first fit method was implemented just for one set of measurement data and just with the Double Gaussian model (AppendixA). In particular, having used a model with three degrees of freedom, three nested loops were implemented to find the optimal parameters. For each iteration the value of one of the parameters is increased and a comparison between the integral of the distribution using the obtained parameters and the one of the BLM signal is performed. If the value found is smaller than a minimum value, the parameters found are stored as optimal parameters. This proceeds until the end of all iterations. For all the other sets of data the profile has been reconstructed through the use of the Lmfit library, using both models. With particular reference to the Double Gaussian model, it was decided to make at first a weighted fit of the beam tails with a Single Gaussian model, since they are the most difficult to fit, in order to have reference values for the parameters of the Gaussian which fits the tails in the Double Gaussian model. Therefore, according to the notation used previously, the initial values choosen for I_2 and σ_2 are those found. These were calculated assuming as constraint on the minimum value for σ_2, σ_1, since the relationships which we expected to be valid are:

$$I_1 > I_2 \quad and \quad \sigma_2 > \sigma_1 \tag{5.6}$$

In addition we have taken into account that the sum of the intensities of both the single gaussians is equal to the integral of the distribution. Instead, for what concerns the Lèvy Student model (8), the constraint imposed is $n > 2$.
The usefulness of the Lmfit library relies on in the fact that, in addition to the fit, it returns a fit-report containing the optimization model used, the chi-square and reduced chi-squared value and it also shows the initial values of the parameters for the fit and best values of the fit parameters found and used to model the profile.

5.3 Beam Profile Reconstruction from the BWS

In order to make a comparison with the reconstructed profile from the BLM signal, the profile generated by the data extracted from the wire scanners was also analyzed. In particular, for both profiles reconstructed with the scan in and scan out, the position of the wire scanner and the amplitude of the BWS signal were observed. In addition, the BWS values for emittance and the β function were also extracted. As the wire makes two crossings through the beam, two measurements are obtained for each parameter. In order to have a unique measurement for each parameter and for each profile, the avarage between the scan in and scan out values has been calculated (8).The emittance value obtained is the one of the normalized emittance, so it has been divided by γ, calculated as $\gamma = E/m_p$, with E energy and m_p proton mass, (0.938 GeV/c^2). Note the parameters of emittance and β function, it was possible to evaluate the value of σ through equation 2.15.

5.4 Comparion between profiles

Having extracted the beam profile data from both the BLM and the BWS, it is possible to compare the plots obtained. In particular, the values of σ were compared, calculated using the formula:

$$\sigma = \sqrt{\frac{\beta\epsilon}{\gamma}} \tag{5.7}$$

where the emittance values are obtained form the BWS (standard instrument used at LHC for emittance measurements). This value is used to compute the beam size at the collimator, using the nominal optics for the β functions.
In order to compare the profiles obtained, a normalization of the data was performed. This was done with respect to both the area, using a pyhton function that integrate along the given axis using the composite trapezoidal rule, and the intensity, dividing each point of the BLM signal by the maximum value of the reconstructed profile trend. The reconstructed shapes were then compared both to each other and to a theoretical Gaussian in order to verify what has been previously stated, that is that the beam tails are overpopulated.

Chapter 6

Measurement Results

Table 6.1 shows the list of scraping measurements that are available for our study. Mosto fo them are from injection measurements. The ones marked as “Full“ are done with single bunches that are completely scraped with the collimators. “Tail“ scans were done with high intensity beams over a smaller scarping range. There is only one set of data available for the scraping at injection in the skew plane, the scraping at flat top and the tail scraping at injection in the horizontal plane.

TABLE 6.1: Data set available

LHC Cycle	Scraping	Beam	Horizontal Plane	Vertical Plane	Skew Plane
Injection	Full	B1	5	2	1
		B2	4	2	1
	Tails	B1	1	-	-
		B2	1	-	-
Flat Top	Full	B1	-	1	-
		B2	-	1	-

6.1 Full Scraping

The first set of data on which the analysis was carried out is from 2017 and it is the result of a scraping of a single-bunch beam at 450 GeV in the horizontal plane (Figure 6.1).

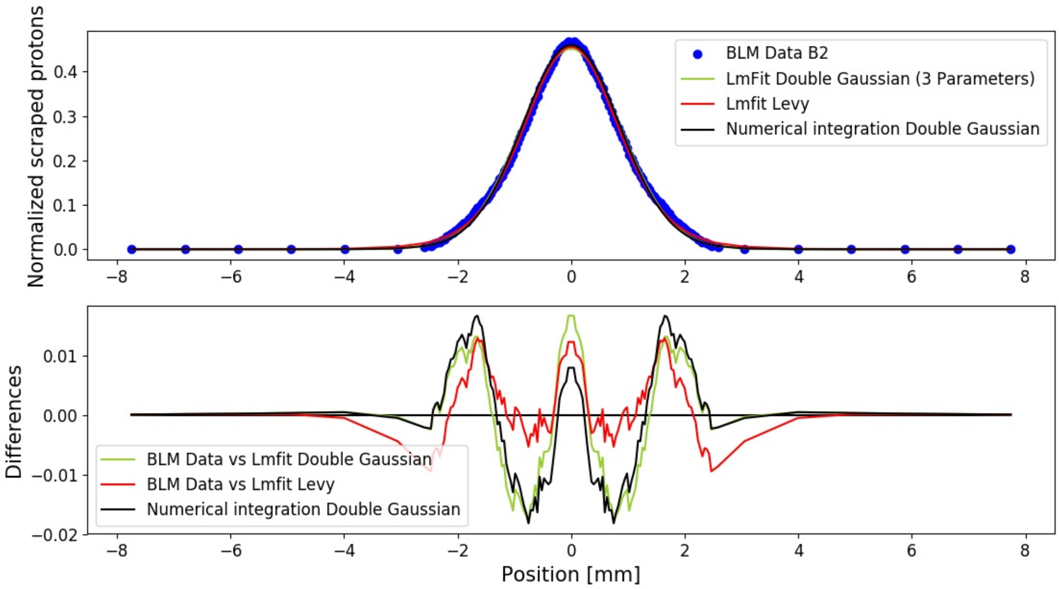

FIGURE 6.1: Horizontal scraping of beam 2 (B2) at injection and fitted profile with both methods: numerical integration and Lmfit library.

It was performed by moving the collimator jaw in steps of 50 μm every 2 seconds. The reconstructed profile shown in Figure 6.1 by the BLM signal, for only beam 2, is represented by blue dots. Overlapped there are the reconstructed profile obtained with both fitting methods explained above: the numerical integration method, implemented only for the Double Gaussian model, and the Lmfit method, applied to both models. With reference to Figure 6.1, the numerical integration method is plotted with a black continuous line, while, the Lmfit method is plotter in green (Double Gaussian) and in red (Lèvy Student).
In order to evaluate which model is better to fit the beam profile, the differences between the BLM data and the fit models were also plotted. It is possible to see, as previously mentioned, that the numerical integration method leads to a larger error in the fit. For this reason, in the subsequent analysis, this method was excluded and it has been decided to implement only the Lmfit method.
The profile has been also plotted in logarithmic scale (Figure 6.2) with error bars based on the background noise of the BLM signal, computed as explained in the Chapter 5.

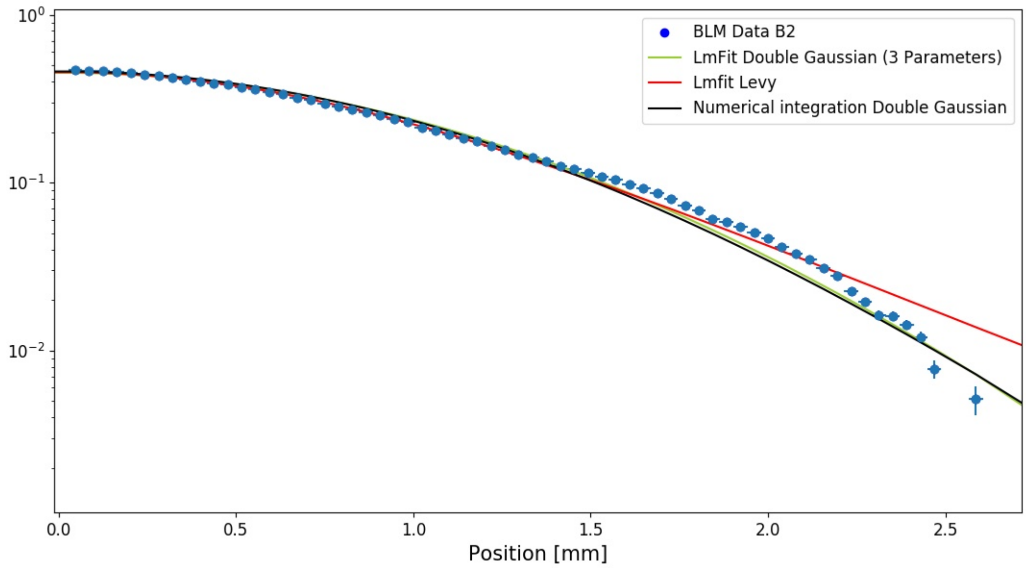

FIGURE 6.2: Horizontal scraping of beam 2 (B2) at injection and fitted profile, in logarithmic scale, with both methods: numerical integration and Lmfit library.

It can be clearly seen that while in the range between 0 and 2 mm 2σ the fit agrees well with the data, tails deviate from the different fits. This is due to the fact that in tails there is a less number of particles and it is closer to the level noise, this makes its analysis very delicate. However, looking at the plot of the differences it turns out that, for this dataset, the model that best fits the beam profile is the Lèvy student.

In order to verify that the implemented script could be extended to other measurements, the analysis was repeated on other data sets.
The analysis presented next concerns data acquired during different moments in 2018. In particular, the ones shown in Figure 9.10 represent a full scraping of beam 1 at injection in the horizontal plane, in which the collimators were moved in step of 50 μm every 5 seconds (in AppendixB the results of the scraping for the beam 2 are shown).

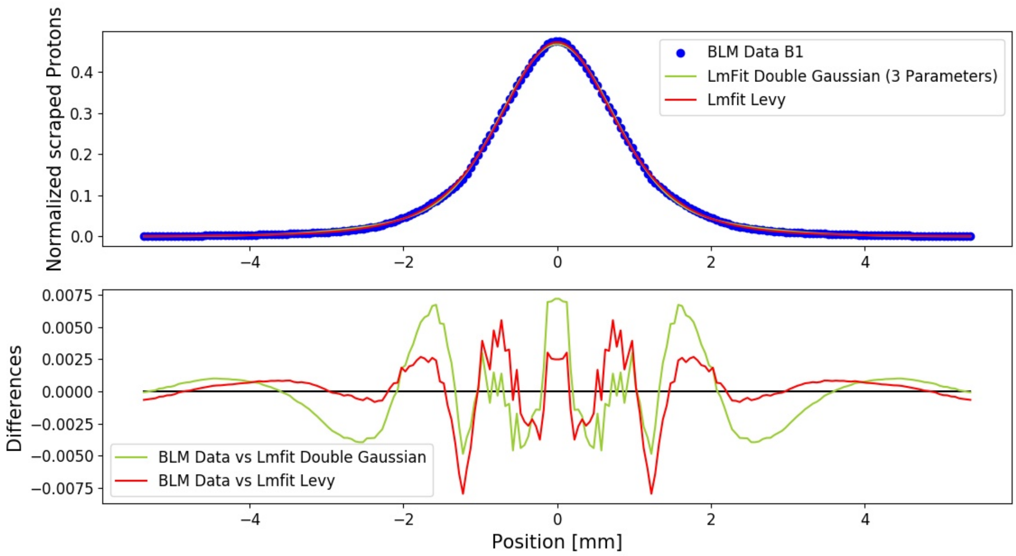

FIGURE 6.3: Horizontal scraping of beam 1 (B1) at injection and fitted profile using only the Lmfit library method. The differences between the BLM data and the profile reconstructed with the Double Gaussian (green) and the Lèvy Student (red) models are also shown.

The logarithmic scale plot (Figure 6.4) shows that the difference of the fit for the tails from the BLM data falls roughly within the error bars. In first analysis, it is therefore possible to conclude that the error is probably due to the noise in the instrument.

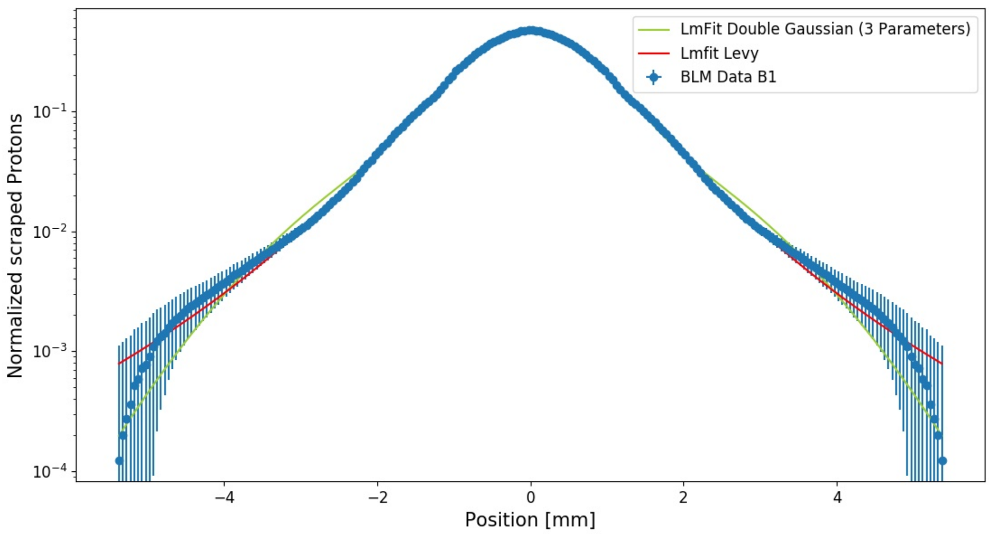

FIGURE 6.4: Horizontal scraping of beam 1 (B1) at injection and fitted profile, in logarithmic scale, using only the Lmfit library method.

Furthermore, a comparison of the reconstructed profile from the BLM, in blue, with the one obtained from the BWS, in orange, was performed. This was done both with respect to the area, on the left, and to intensity, on the right (Figure 6.5).

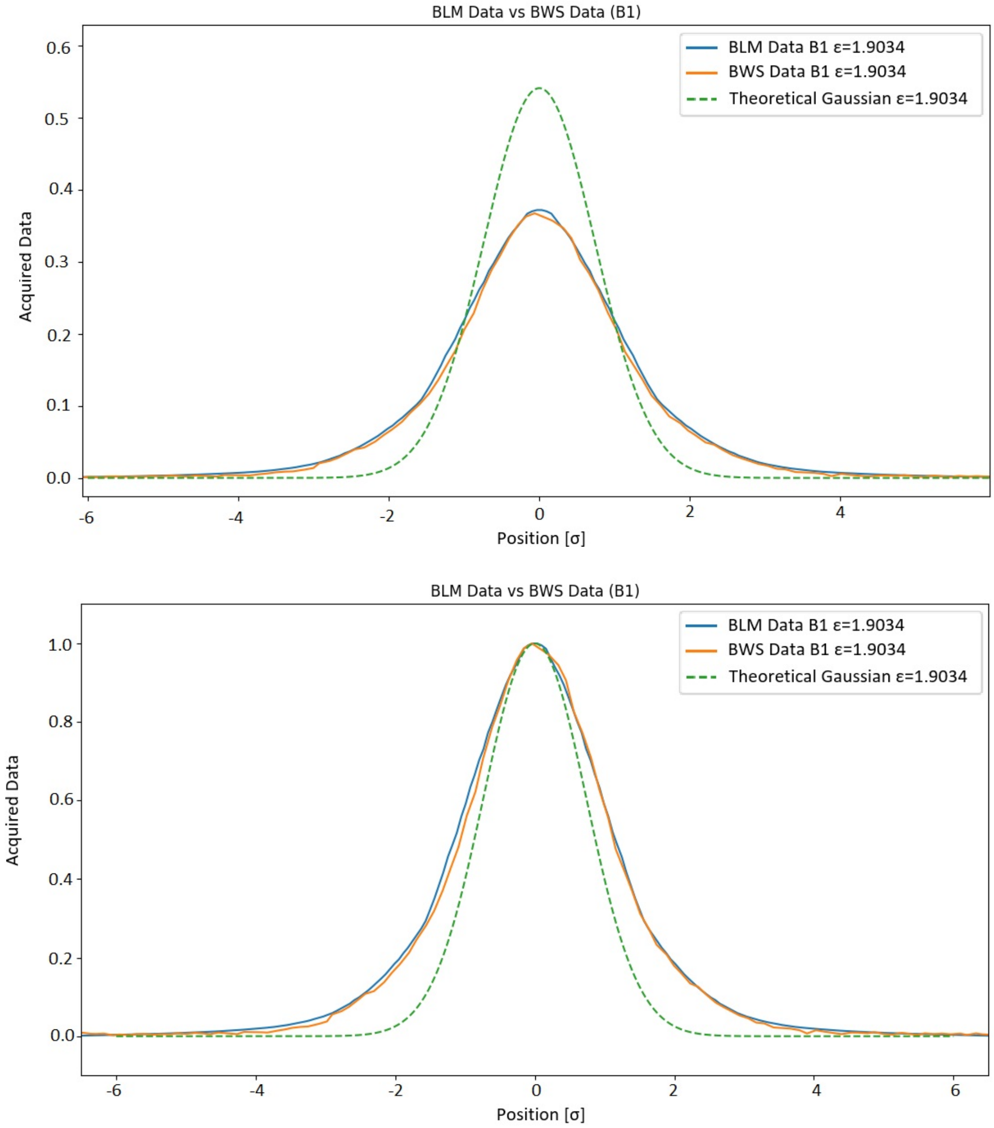

FIGURE 6.5: Profile of B1 reconstruct from BLM (blue) and BWS (orange) overlapped to the theoretical Gaussian. The data were normalized with respect to the area (up) and to the intensity (down).

The results were plotted overlapped with a theoretical Gaussian whose variance value has been evaluated using the value of emittance extracted from the BWS, which in this case is equal to $1.9034\mu m$.
From the plots obtained, it can be verified that the trends of the beam profile, reconstructed with the BLM and the BWS, agree well. Moreover it can be seen, as explained before, that while the fit of the core is almost good, the tails are overpopulated with respect to a theoretical gaussian.

A collimator scraping, under the same conditions, was also done in the vertical plane (Figure 6.6). Unlike the previous case, in which from the plot of the differences between the BLM data and the profile reconstructed, the Lèvy Student model seems to fit the profile better, the best model resulting from this analysis turns out to be the Double Gaussian. But, in order to decide which is the best one, the chi-square values will be analyzed later.

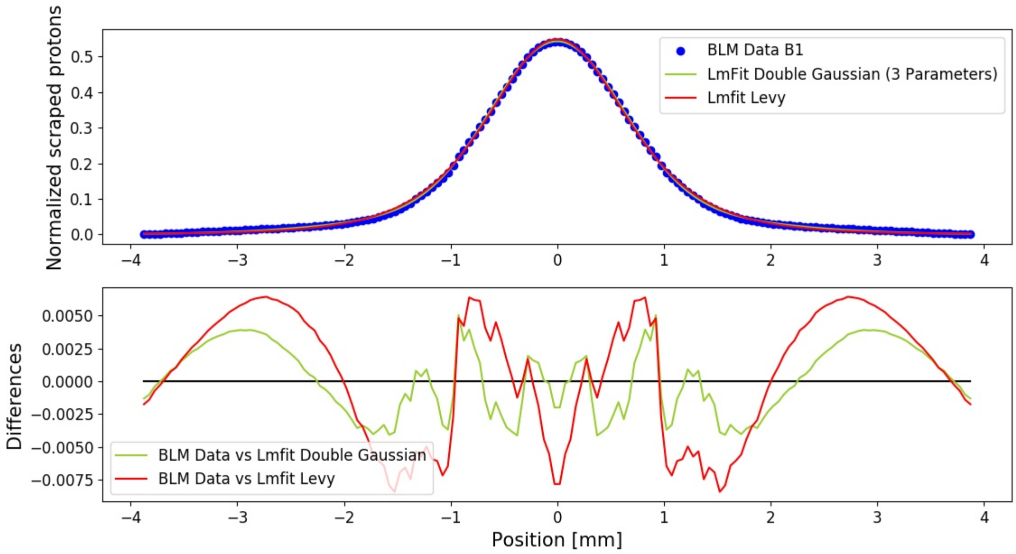

FIGURE 6.6: Vertical scraping of B1 at injection and fitted profile using only the Lmfit library method. The differences between the BLM data and the profile reconstructed with the Double Gaussian (green) and the Lèvy Student (red) models are also shown.

Also in this case the profile has been plotted in logarithmic scale (the plots related to beam 2 can be found in in the AppendixB).

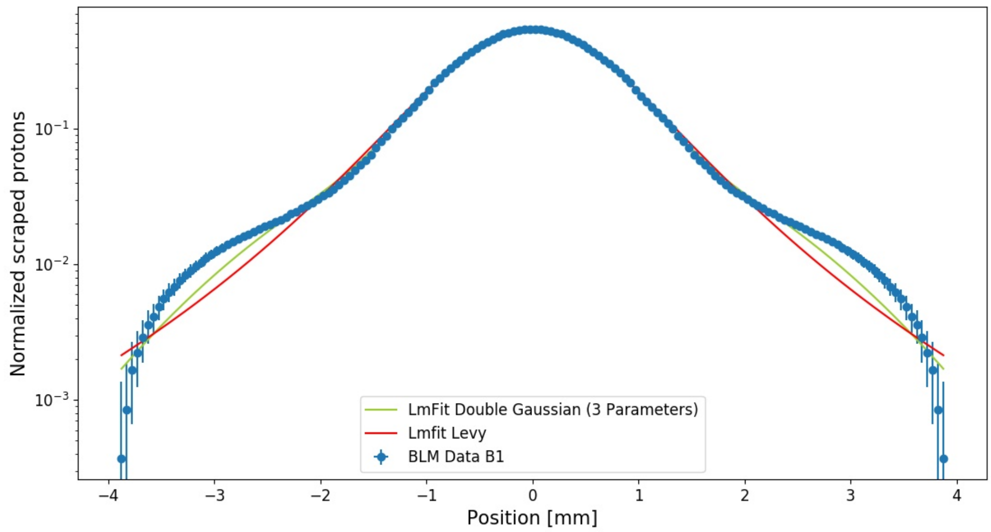

FIGURE 6.7: Vertical scraping of B1 at injection and fitted profile, in logarithmic scale, using only the Lmfit library method.

One can se that the profile obtained from the collimator scraping and with the profile obtained using the BWS differ more than in the horizontal plane (Figure 6.8). To address this issue, different hypotheses have been made, including that in the vertical plane the size of the beam is smaller than that in the horizontal plane, so probably the resolution of the BWS is not sufficient enough to succeed, at every step made by the wire, to count the correct number of intercepted particles. However, in first analysis it has not been possible to deep this issue, so it is still under investigation.

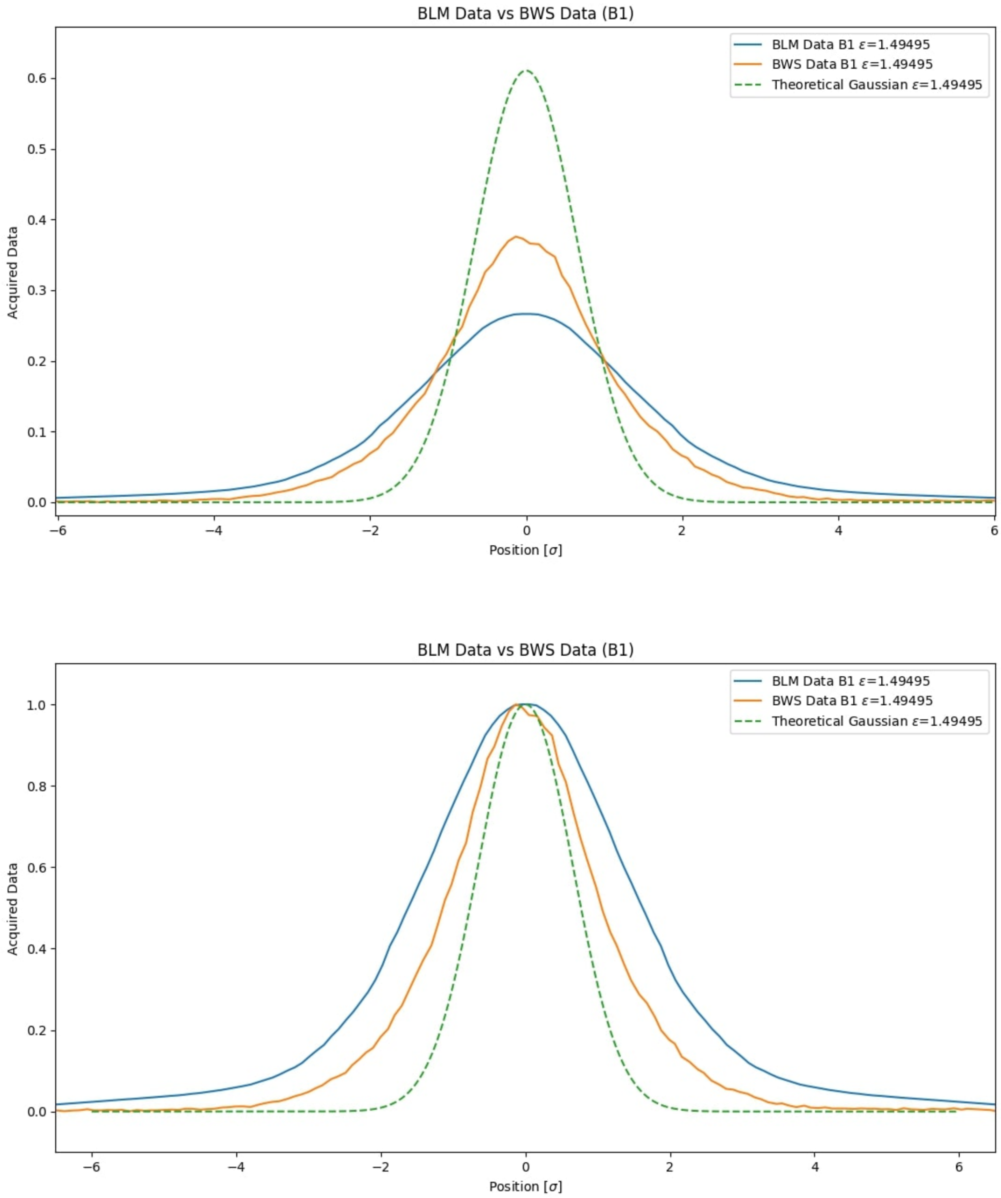

FIGURE 6.8: Profile of B1 reconstruct from BLM (blue) and BWS (orange) overlapped to the theoretical Gaussian. The data were normalized with respect to the area (up) and to the intensity (down).

In addition to the scraping shown, a scraping of beam 1 in the skew plane has been performed for the first time at the injection (the results of beam 2 are in the AppendixB).

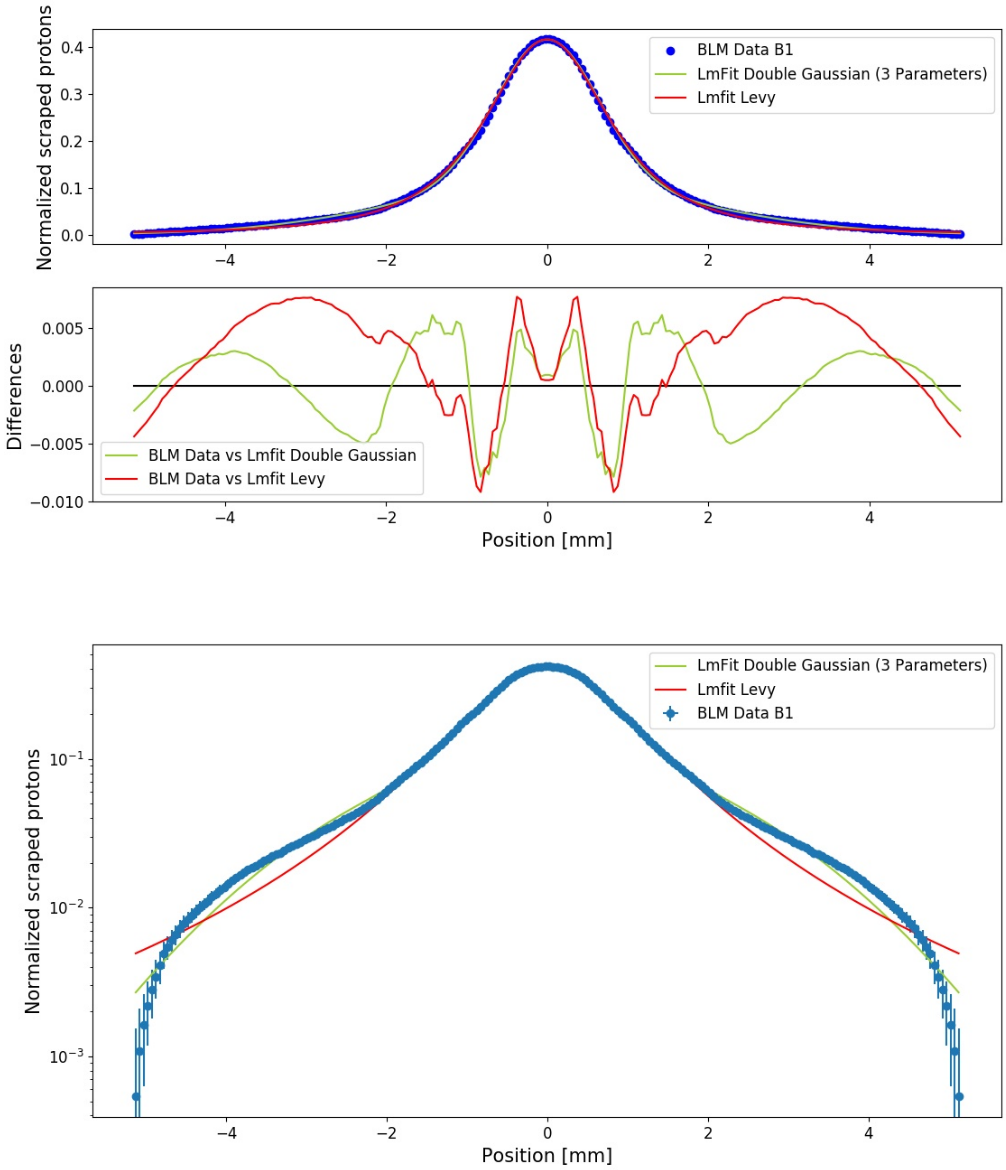

FIGURE 6.9: Skew scraping of B1 at injection and fitted profile using only the Lmfit library method. The differences between the BLM data and the profile reconstructed with the Double Gaussian (green) and the Lèvy Student (red) models are also shown. Both linear (up) and logarithmic scale (down) are shown.

Since the wire scanners exists only in the vertical and horizontal plane, it was not possible to make a direct comparison with the profile reconstructed by the BWS. We could however use the BWS to extract the emittance values in the horizontal and vertical planes, calculate the *sigma* through the equation

$$\sigma = \sqrt{(\sigma_H cos(45°))^2 + (\sigma_V sin(45°))^2} \tag{6.1}$$

and then use it to draw the shape of the beam profile.

The analysis carried out for the vertical scraping, presented above, has also been performed for the data obtained from scraping at flat top in the vertical plane.

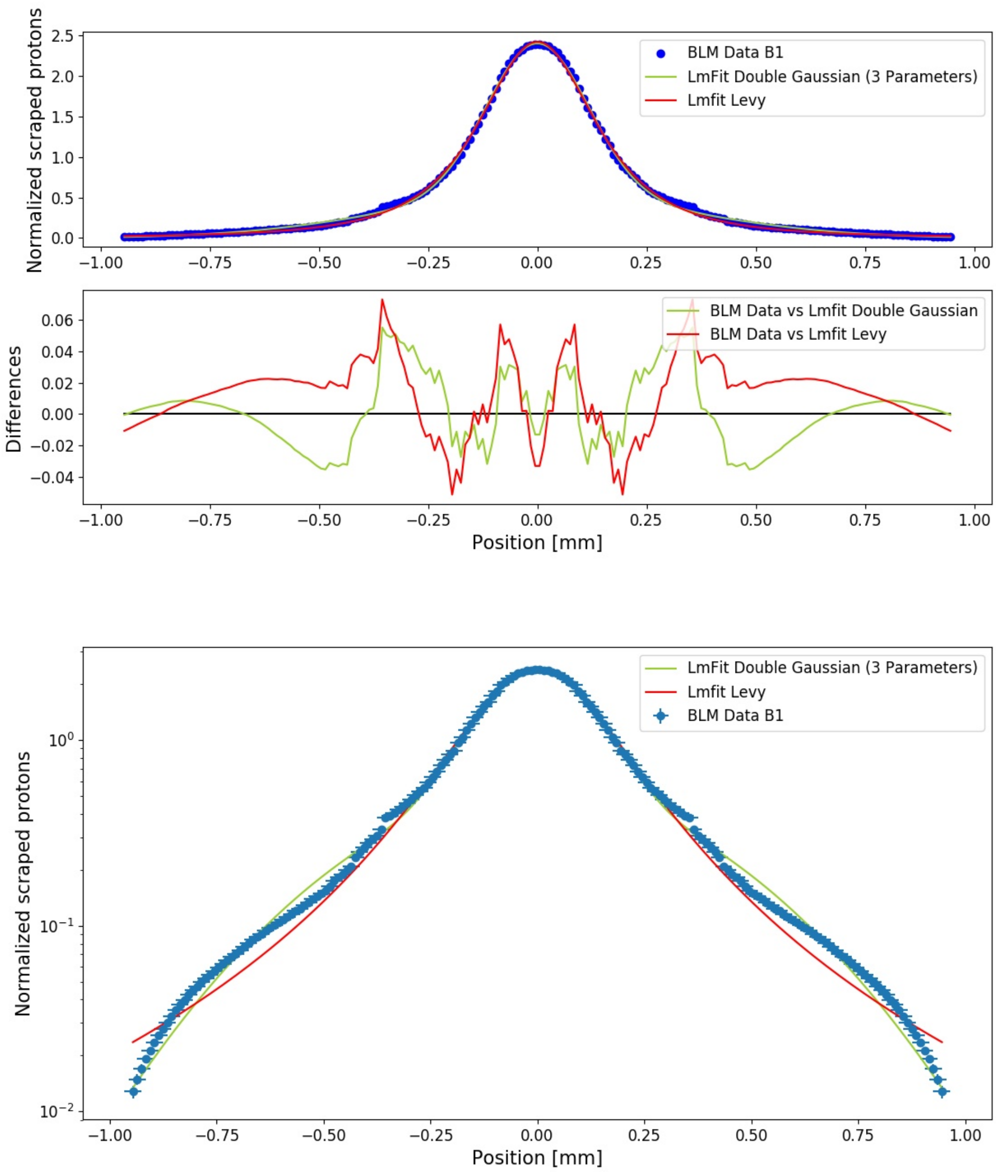

FIGURE 6.10: Vertical scraping of B1 at flat top and fitted profile using only the Lmfit library method. The differences between the BLM data and the profile reconstructed with the Double Gaussian (green) and the Lèvy Student (red) models are also shown. Both linear (up) and logarithmic scale (down) are shown.

In this case, we found a problem of data acquisition from the BLM. This is due to the fact that during the scraping the frequency of movement of the collimator jaw has been changed, in particular we have gone from 3 seconds to 5 seconds. A longer waiting time in the collimator movement involves a process of repopulation of the tails, due to the diffusion process, which causes the level of particles to be higher when compared to what is expected when the next collimator steps takes place. Also in this case a comparison was made with the profile extracted from the BWS:

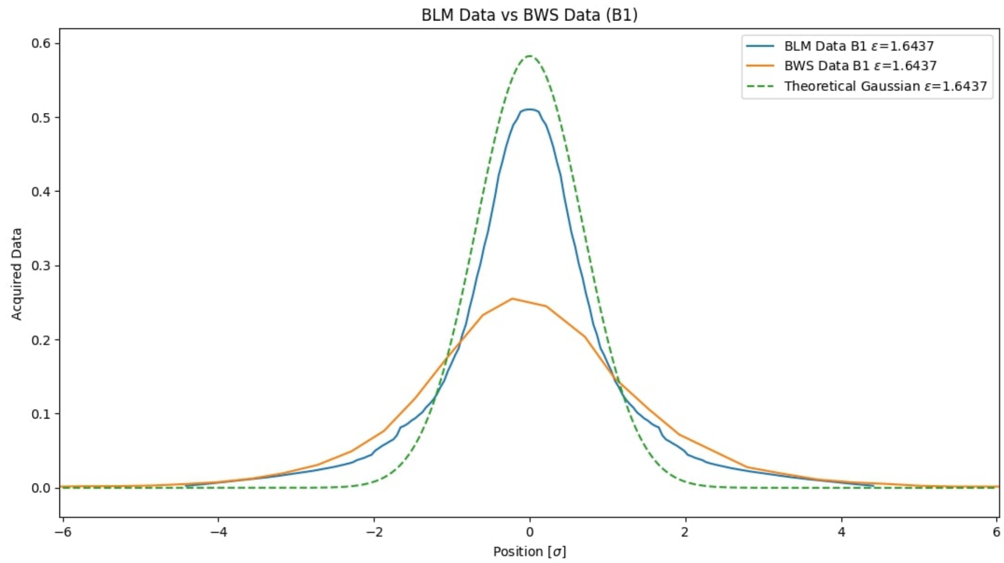

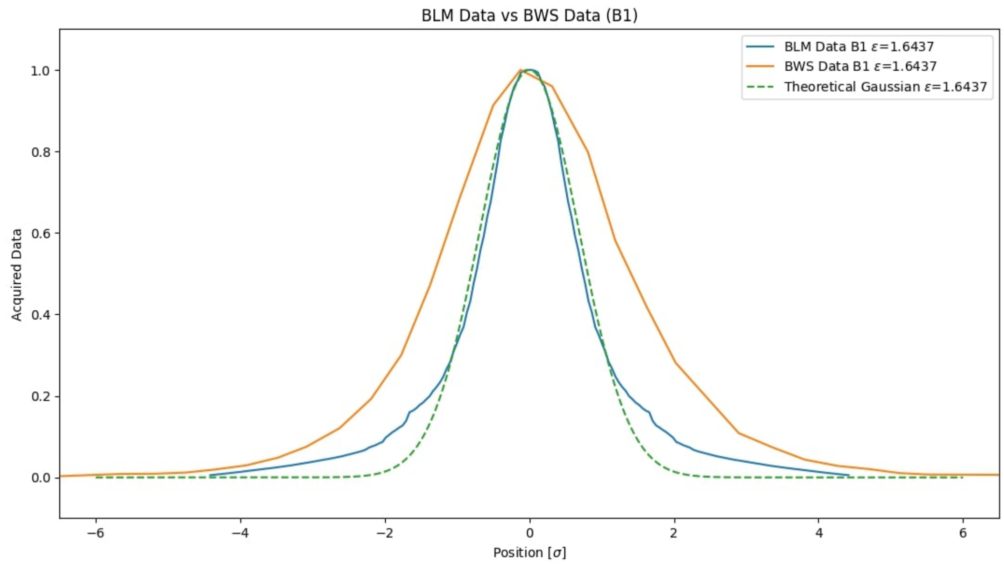

FIGURE 6.11: Profile of B1 reconstruct from BLM (blue) and BWS (orange) overlapped to the theoretical Gaussian. The data were normalized with respect to the area (up) and to the intensity (down).

Also in this case we have obtained the same conclusions: there is a misalignment between the profiles reconstructed with the two instruments. However, in both cases, the tails turn out to be overpopulated with respect to the theoretical gaussian. From this first analysis done, it can be seen that the script implemented works for both the LHC cycles: injection and flat top. In addition, it turns out to be model indipendent, so it can be used to repeat the same analysis with a different mathematical model.

6.2 Tails Scraping

The results shown untill now are related to full scraping, but also a tail scraping at injection in the horizontal plane has been performed.

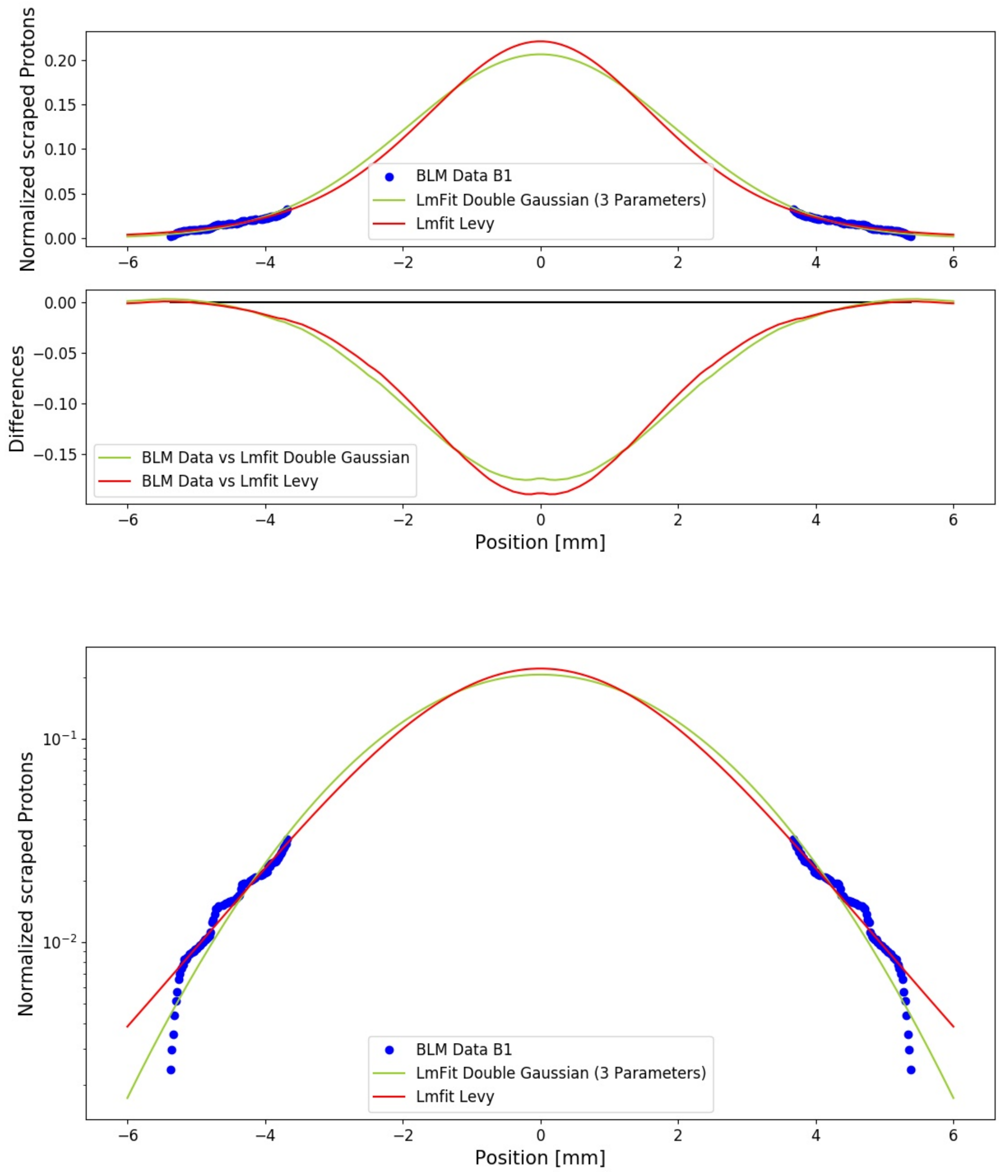

FIGURE 6.12: Tails scraping at injection and fitted profile using the Lmfit method.

In this case we should take into account that the parameters extracted from the beam are not those useful to reconstruct the full beam introduciong them in the models choosen. This is due to the fact that the fit only takes into account the data extracted from the BLM related to the tails, therefore we are missing informations about the core. This it can be clearly seen if we compare the fitted profile with the ones reconstructed through BWS.

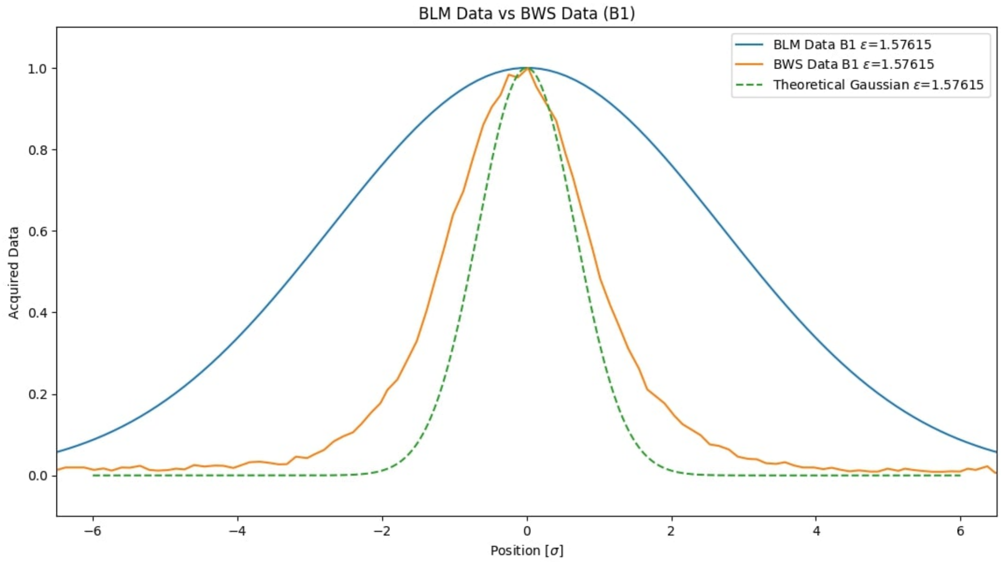

FIGURE 6.13: Profile of B1 reconstruct from BLM (blue) and BWS (orange) overlapped to the theoretical Gaussian. The data are normalized with respect to the intensity.

The profile reconstructed from the BWS (in orange) shows that the core follows quite the shape of a single Gaussian, while the tails are overpopulated, the profile fitted from the data extracted from the BLM differs widely from this trend.

6.3 Scraping after blow-up

All the data analyzed right now were $1Hz$ data, the result that will be shown in this section are instead two sets of $100Hz$ data. The advantage of this analysis lies in the fact that in this case the information obtained turns out to be more detailed. This is due to the fact that, while in the previous cases we obtained only one point between one collimator step and the next one, in the case of data at $100Hz$ we obtain more points for each step.
In the first case, that is a horizontal scraping at injection, the collimator was moved in steps of 50 μm every 2 seconds. Below are shown the results:

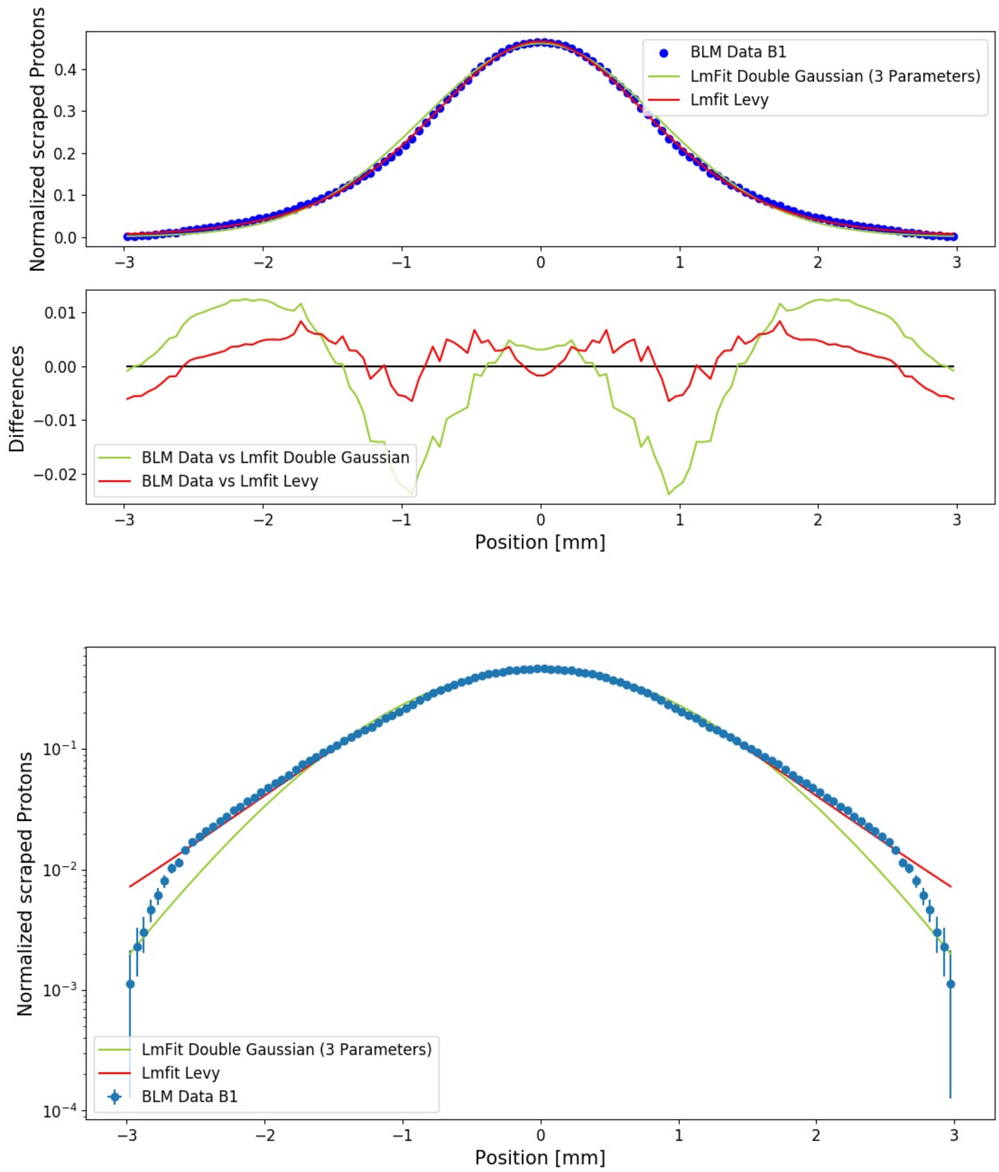

FIGURE 6.14: Horizontal scraping of of a blown-up bunch and fitted profile using only the Lmfit library method. The differences between the BLM data and the profile reconstructed with the Double Gaussian (green) and the Lèvy Student (red) models are also shown. Both linear (up) and logarithmic scale (down) are shown ($100Hz$ data).

The results obtained confirm what has been asserted in the case of 1 Hz data in the horizontal plane. The trend of the data of the BLM follows quite the profile with the Lèvy Student model. This is quite evident from the plot of the differences, in which the continuous line in red differs slightly from the zero. In addition, this analysis allows to show how the script implemented works with different tipe of data.

A second scraping has been performed under the same conditions, but this time it has been done on a blown-up bunch, performed via a white noise excitation using the *LHC Transverse Damper (ADT)*, with an increase for the emittance of a factor 4. The results obtained are showen below:

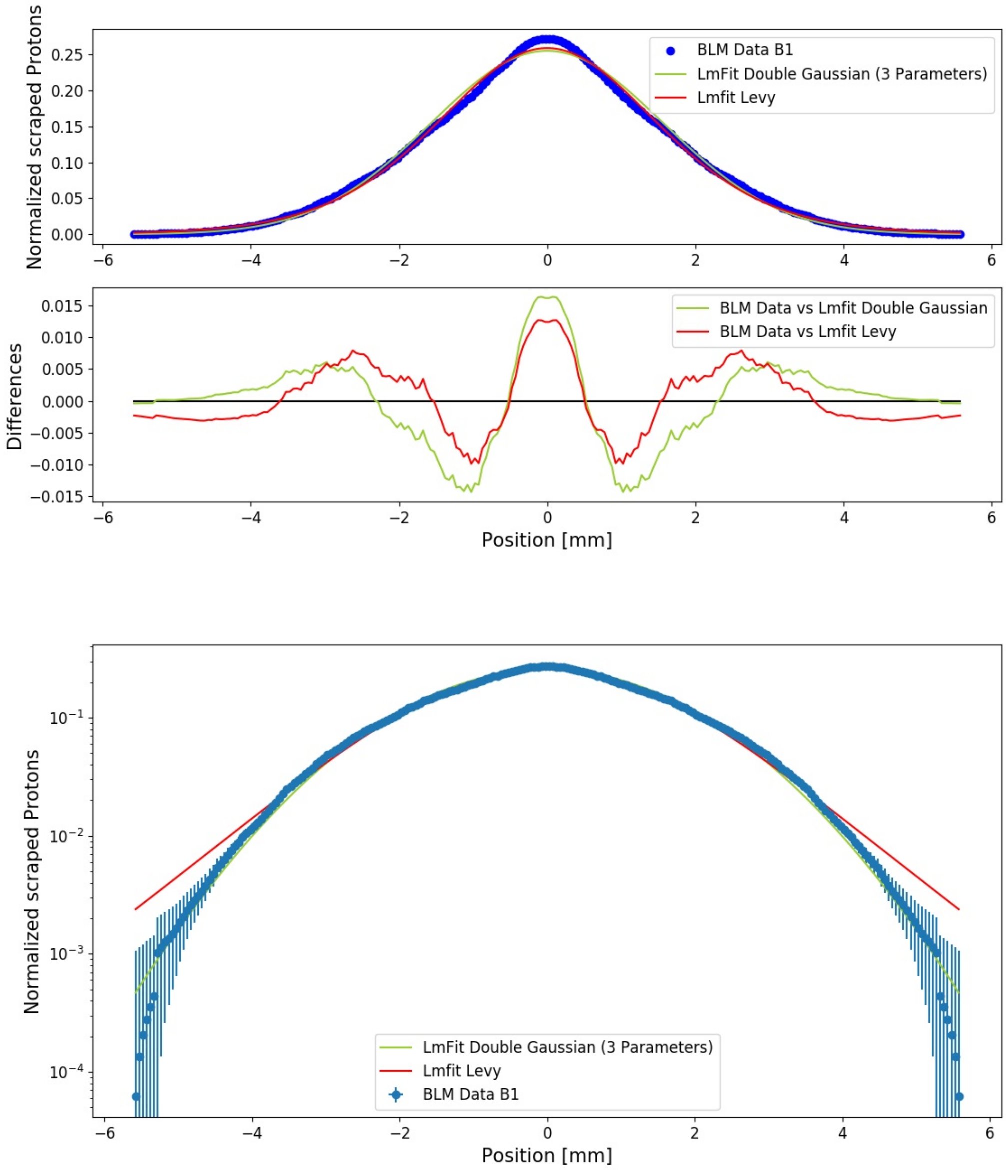

FIGURE 6.15: Horizontal scraping of a blown-up bunch and fitted profile using only the Lmfit library method. The differences between the BLM data and the profile reconstructed with the Double Gaussian (green) and the Lèvy Student (red) models are also shown. Both linear (up) and logarithmic scale (down) are shown ($100Hz$ data).

This is an example of manipulating the beam and the distribution turns out to be completely different from the normal one: it has a more triangular shape. This makes harder to fit the distribution with the models used in previous analyzes, indeed the fit doesn't reach the peak of the distribution obtained from the BLM. Therefore, it turns out that the implemented script is not efficient enough to work under these conditions.

6.4 Parameters analysis

The analysis of the results of the different scraping done allows to extract some interesting considerations.
From the plots of the profile reconstructed with the BLM data, it has been possibile to evaluate the amount of particles in the tails beyond 2σ, 3σ and 4σ. The σ to which we refer is the one of the distribution, evaluated using the emittance value obtained from the BWS.

TABLE 6.2: Fraction of particles in the horizontal plane evaluated beyond 2σ, 3σ and 4σ.

DATA ACQUISITION	BEAM	SCRAPING	BEYOND 2σ	BEYOND 3σ	BEYOND 4σ
30/07/2018	B1	FULL	18%	5.3%	2%
			22%	7.7%	3%
			24%	8%	3%
19/09/2018	B1	FULL	25%	8%	1.9%
30/07/2018	B2	FULL	21%	6%	2%
			25%	10%	3%
			19%	6%	2%

TABLE 6.3: Fraction of particles in the vertical plane evaluated beyond 2σ. 3σ and 4σ.

DATA ACQUISITION	BEAM	SCRAPING	BEYOND 2σ	BEYOND 3σ	BEYOND 4σ
30/07/2018	B1	FULL	34%	13%	6%
			27%	9%	4%
30/07/2018	B2	FULL	30%	9%	3%
			29%	10%	3%

TABLE 6.4: Fraction of particles in the skew plane evaluated beyond 2σ. 3σ and 4σ.

DATA ACQUISITION	BEAM	SCRAPING	BEYOND 2σ	BEYOND 3σ	BEYOND 4σ
30/07/2018	B1	FULL	15%	7%	3.6%
30/07/2018	B2	FULL	19%	10%	3.7%

A similar analysis was done in the past Burkart, 2009 from which it turned out that the fraction of particles beyond 4σ was 2.7% for the horizontal plane, 1.9% and 3.6% for the vertical and skew plane respectively. From the results obatind we can see that we have found similar values in the horizontal plane, but in the vertical plane the fraction of particles is larger, while for what concern the skew plane we can't say more since only one set of data is available.
In addition, the paramters found from the fits were evaluated in the horizontal, verticale and skew planes.

TABLE 6.5: Values of the parameters, of both Double Gaussian and Lèvy Student models, extracted from the fitted profile in the horizontal plane.

DATA ACQUISITION	BEAM	SCRAPING	MODEL					
			DOUBLE GAUSSIAN				LEVY STUDENT	
			I_1	I_2	σ_1	σ_2	n	a
25/07/2018	B1	TAILS	0.69	0.3	1.99	1.96	7.82	5.18
30/07/2018	B1	FULL	0.66	0.33	0.76	1.68	4.14	1.76
		FULL	0.62	0.37	0.76	1.73	3.56	1.68
		FULL	0.67	0.32	0.79	1.83	3.81	1.76
19/09/2018	B1	FULL	0.7	0.3	1.72	2.14	6.74	4.53
		FULL	0.7	0.3	1.65	1.72	9.41	4.92
15/09/2017	B2	FULL	0.59	0.4	0.83	0.97	8.52	2.48
25/05/2018	B2	TAILS	0.85	0.14	1.88	2.21	99.99	19.11
30/07/2018	B2	FULL	0.72	0.27	0.77	1.7	4.67	1.83
		FULL	0.61	0.38	0.77	1.52	4.88	1.99
		FULL	0.63	0.36	0.68	1.69	3	1.39

TABLE 6.6: Ratio between the intensities and variances values of the Double Gaussian model, obtained from the fits in the horizontal plane.

BEAM	DOUBLE GAUSSIAN MODEL	
	I_1/I_2	σ_1/σ_2
B1	2.1	1.01
	2	2.33
	1.67	2.27
	2.09	2.31
	2.33	1.24
	2.33	1.04
B2	1.47	1.16
	6.07	1.17
	2.66	2.2
	1.6	1.97
	1.75	2.48

TABLE 6.7: Values of the parameters, of both Double Gaussian and Lèvy Student models, extracted from the fitted profile in the vertical plane.

DATA ACQUISITION	BEAM	SCRAPING	MODEL					
			DOUBLE GAUSSIAN				LEVY STUDENT	
			I_1	I_2	σ_1	σ_2	n	a
30/07/2018	B1	FULL	0.69	0.3	0.92	2.07	4.1	2.09
		FULL	0.72	0.27	0.87	2.14	4.11	1.96
		FULL	0.54	0.45	0.17	0.52	2	0.31
30/07/2018	B2	FULL	0.79	0.2	1.05	2.2	7.36	3.06
		FULL	0.62	0.37	0.89	1.81	4.53	2.2
		FULL	0.77	0.22	0.24	0.59	4.96	0.58

TABLE 6.8: Ratio between the intensities and variances values of the Double Gaussian model, obtained from the fits in the vertical plane.

BEAM	DOUBLE GAUSSIAN MODEL	
	I_1/I_2	σ_1/σ_2
B1	2.3	2.25
	2.66	2.45
	1.2	5.05
B2	3.95	2.09
	1.67	2.03
	3.5	2.45

TABLE 6.9: Values of the parameters, of both Double Gaussian and Lèvy Student models, extracted from the fitted profile in the skew plane.

DATA ACQUISITION	BEAM	SCRAPING	MODEL					
			DOUBLE GAUSSIAN				LEVY STUDENT	
			I_1	I_2	σ_1	σ_2	n	a
30/07/2018	B1	FULL	0.82	0.17	0.71	2.07	2	0.97
30/07/2018	B2	FULL	0.76	0.23	0.72	1.73	4.62	1.67

TABLE 6.10: Ratio between the intensities and variances values of the Double Gaussian model, obtained from the fits in the skew plane.

BEAM	DOUBLE GAUSSIAN MODEL	
	I_1/I_2	σ_1/σ_2
B1	4.82	2.91
B2	3.3	2.4

The tables show that all the parameters, obtained from the full scraping at injection, respect the constrain of the models. However, there are some values that differ and are those related to the tails scraping and the scraping after the blow-up, which can not be compared with the other sets of data. For each plane the ratio between the parameters has been evaluated, from which we can see that the ratio between the sigma is about 2, while in the past it was estemated to be 1.8 (Burkart, 2009).
From the analysis made and from a check of the chi-squared values for both the chosen models it was possible to fill the following tables, from which it is possible to estabilish which is the chi-square value, that provides a quality factor for the fit, closer to zero.

TABLE 6.11

DATA ACQUISITION	SCRAPING	BEAM	MODEL	
			DOUBLE GAUSSIAN	LEVY STUDENT
15/09/2017	FULL	B2	0.0132	$3.5722e-05$
25/05/2018	TAILS	B1	0.0010	$2.3858e-04$
		B2	$8.3143e-05$	$8.3989e-05$
30/07/2018	FULL	B1	0.0014	$7.3229e-04$
		B2	0.0018	$4.4269e-04$
		B1	$8.6894e-04$	$9.0674e-04$
		B2	0.0026	$1.4804e-05$
		B1	$8.2711e-04$	$8.2907e-04$
		B2	0.0034	0.0010
19/09/2018	FULL	B1	0.0415	0.0536
		B2	0.0394	0.0187

TABLE 6.12: Chi-squared values extracted from the fitted model in the vertical plane, through the use of Lmfit library.

DATA ACQUISITION	SCRAPING	BEAM	MODEL	
			DOUBLE GAUSSIAN	LEVY STUDENT
30/07/2018	FULL	B1	$4.6728e-04$	0.0015
		B2	2.2359	$8.2438e-04$
	FULL	B1	$3.5398e-04$	0.0012
		B2	$7.8406e-04$	$3.1245e-05$
	FULL	B1	0.0415	0.0536
		B2	0.0394	0.0187

TABLE 6.13: Chi-squared values extracted from the fitted model in the skew plane, through the use of Lmfit library.

DATA ACQUISITION	SCRAPING	BEAM	MODEL	
			DOUBLE GAUSSIAN	LEVY STUDENT
30/07/2018	FULL	B1	0.0066	0.0335
		B2	0.0028	0.0014

It's clear that for the scraping in the horizontal plane, the best model for the fit of the beam distribution turns out to be the Lèvy Student, while in the vertical plane the double gaussian. As for the skew plan, on the other hand, we can not say much since there is only one case available. However, there is a lower statistic and it would be useful to have more data sets for each case in order to extrapolate a certain conclusion.

In order to have a measure quantifying the dispersion of the values, the standard deviation was evaluated for the parameters of the fitting models at injection. This was not done for the skew plan as there was only one data set available.

TABLE 6.14: Average and standard deviation evaluated on the parameters obtained from the fitted profile, computed using the Double Gaussian model. The values find can be used as reference parameters of the proposed model.

SCRAPING	BEAM	AVERAGE $\pm$ STANDARD DEVIATION			
		DOUBLE GAUSSIAN			
		I_1	I_2	σ_1	σ_2
HORIZONTAL	B1	0.66 ± 0.028	0.33 ± 0.025	1.01 ± 0.411	1.85 ± 0.178
	B2	0.64 ± 0.049	0.35 ± 0.049	0.76 ± 0.053	1.47 ± 0.297
VERTICAL	B1	0.71 ± 0.015	0.29 ± 0.085	0.9 ± 0.025	2.11 ± 0.034
	B2	0.71 ± 0.085	0.29 ± 0.085	0.97 ± 0.08	2.01 ± 0.195

TABLE 6.15: Average and standard deviation evaluated on the parameters obtained from the fitted profile, computed using th eLèvy Student model. The values find can be used as reference parameters of the proposed model.

SCRAPING	BEAM	AVERAGE $\pm$ STANDARD DEVIATION	
		LEVY STUDENT	
		n	a
HORIZONTAL	B1	4.56 ± 1.273	2.46 ± 1.211
	B2	5.27 ± 2.014	1.92 ± 0.398
VERTICAL	B1	4.11 ± 0.005	2.03 ± 0.064
	B2	5.95 ± 1.415	2.63 ± 0.43

TABLE 6.16: Ratio between the calculated averages of the intensities and variances of the Double Gaussian model.

BEAM	DOUBLE GAUSSIAN MODEL	
	I_1/I_2	σ_1/σ_2
B1	2	1.83
B2	1.82	1.93
B1	2.44	2.34
B2	2.44	2.07

It can be seen that, in most cases, the standard deviation is small enough to say that the parameters are quite similar and also the values between beam 1 and beam 2 are quite close to each other. We have to take into account that the smaller values for the standard deviation in the vertical plane are due to the fact that we have less data available than the horizontal plane, on which to compare. The values shown in these tabels can be considered as reference parameters for the final model that we are proposing.

Chapter 7

Conclusions and Further Work

This study has been carried out in order to find a mathematical model to describe accurately measurements of the beam profile in the LHC and estabilish reference description of beam population. In order to achieve the objective, different scans with single bunches have been performed with TCP in IR7 in the horizontal, vertical and skew plane in different stages of the LHC cycle, allowing the evaluation of the particle distribution in the transverse plane. The data collected have been used to reconstruct the beam profile from the BLM signal. In addition, a comparison with the profile reconstructed through the BWS has been made in order to be able to detect the errors that could be caused by the extraction and manipulation of data through the tools.
A new set of tools has been created, more detailed than those implemented in the past, to find a mathematical model able to fit the beam profile. The script is model independent, which allows the analysis to be extended to other types of models. The models on which the analysis has been carried on are Double Gaussian and Lèvy Student. Through a graphical comparison and the evaluation of the chi-square values, it is clear that the Lèvy model is better suited to the fit of the beam profile in the horizontal plane, while in the vertical one the best model is the double Gaussian. With reference to the last model, the ratio between the variance values of the two Gaussians, which until now has been estimated to be equal to 1.8, is approximately equal to 2. This indicate that the measurements done in Run II are quite consistent with what had been founded in the Run I. The fraction of particles in the tails over 4σ has also been evaluated, from which it has obtained that in the horizontal plane it is in a range between 2% and 3%, while in the vertical plane between 3% and 6%. A statistical analysis was carried out on the available data from which it was possible to extract the reference values of the parameters of the selected models, which are able to work correctly with a small error.
One of the future developments of this could be to test new models to see if they better fit the beam profile, in particular the quasiparabolic distribution that is suited to deal with truncated tails, satisfying the additional constraint of providing a smooth distribution function at the location where it becomes zero. In addition, a valid method could be found for assinging weights to data so that we can perform weighed analyzes. And other development of this study colud be to check the fraction of particles from the model fitted and we expect that they should be quite close to the ones evaluated from the distribution of the BLM data and shown in the previous tables. Finally, the profile obatined from the BLM and BWS could be compared with the one extracted from other instruments, like for example the synchrotron light monitor, in order to understand which one is less accurate where there is a relevant difference between the curves, like in the vertical plane.

Chapter 8

APPENDIX A

Following are some of the functions implemented in the script.

8.1 Collimator Position

The function plots the position of the collimator as a function of time:

```
def posColUSH(t01,t02):
    posUSB1 = "TCP.C6L7.B1:MEAS_MOTOR_LU"
    posUSB2 = "TCP.C6R7.B2:MEAS_MOTOR_LU"
    t1 = convertTime(t01)
    t2 = convertTime(t02)
    dataUSB1=db.get([posUSB1],t1,t2)
    dataUSB2=db.get([posUSB2],t1,t2)
    tt_POSUSB1, vv_POSUSB1 = dataUSB1[posUSB1]
    tt_POSUSB2, vv_POSUSB2 = dataUSB2[posUSB2]
    plotPosUSB1 = plt.plot_date(epoch2num(tt_POSUSB1+2*3600),vv_POSUSB1,
                  '-',color='lime',label='Up Stream Horizontal B1')
    plotPosUSB2 = plt.plot_date(epoch2num(tt_POSUSB2+2*3600),vv_POSUSB2,
                  '--',color='green',label='Up Stream Horizontal B2')
    return plotPosUSB1, plotPosUSB2
```

8.2 Numerical Integration Method

The function searches for the optimal parameters of the model by comparing the two integrals considered in the numerical integration method.

```
I1, I2, sigma1, sigma2 = 1.0, 1.0, 1.0, 1.0
hVec = []
I1Vec = []
I2Vec = []
hMin = 1
```

```
    for k in range(10):
sigma2 = 0.01*(k+1)+ 1.5
for l in range(10):
sigma1 = 0.01*(l+1) + 1.5
for m in range(10):
I1 = 0.1*(m+1)
for j in range(10):
I2 = 0.1*(j+1)
h = 0
for i in range(npairs):
startPos = 50+i # starting position in index (equiv to time)
endPos = 51+i # ending position in index (equiv to time)

startX = colPosmm[startPos]
endX = colPosmm[endPos]
h += (myIntBLM(startPos,endPos)-myInt(startX,endX,npoints,I1,I2,sigma1,sigma2))**2

if h < hMin:
hMin = h
I1min = I1
I2min = I2
sigma1min = sigma1
sigma2min = sigma2
hVec.append(h)
I1Vec.append(I1)
I2Vec.append(I2)
```

8.3 Double Gaussian Model

The function implements the function of the Double Gaussian model, with three parameters of freedom.

```
def DGauss3Par(x,I2,sigma1,sigma2):
I1 = area2 - I2
return (I1/np.sqrt(2*np.pi*(sigma1**2)))*np.exp(-(x*x)/(2*sigma1*sigma1))
       + (I2/np.sqrt(2*np.pi*(sigma2**2)))*np.exp(-(x*x)/(2*sigma2*sigma2))
```

8.4 Lèvy Student Model

The function implements the function of the Lèvy Student model.

```
def Levy(x, n, a):
    num1 = gamma((n+1)/2)
    den1 = gamma(1/2)*gamma(n/2)
    num2 = a**n
    den2 = ((x**2)+(a**2))**((n+1)/2)
    return (num1/den1)*(num2/den2)
```

8.5 Avergae of emittance and β values

The function implements the function that calculates the average between the emittance and *beta* values extracted from the BWS.

```
emit1 = (vv_emitIn[0,0] + vv_emitOut[0,0])/2
beta1 = (vv_betaIn[0] + vv_betaOut[0])/2
```

Chapter 9

APPENDIX B

9.1 Scraping At Injection

The plots show the result of the scraping of B2, in the horizontal plane, performed during 2018.

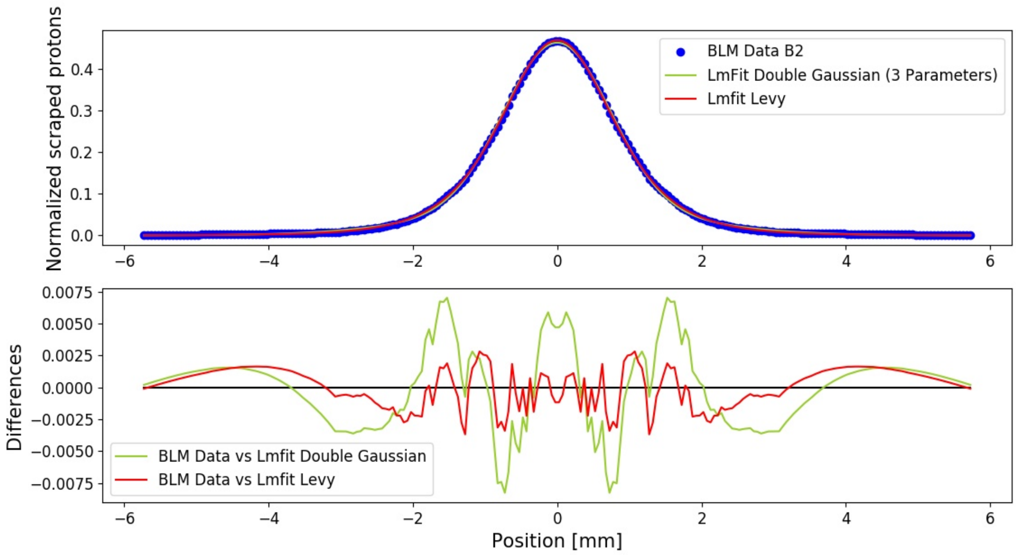

FIGURE 9.1: Horizontal scraping of B2 at injection and fitted profile using only the Lmfit library method. The differences between the BLM data and the profile reconstructed with the Double Gaussian (green) and the Lèvy Student (red) models are also shown.

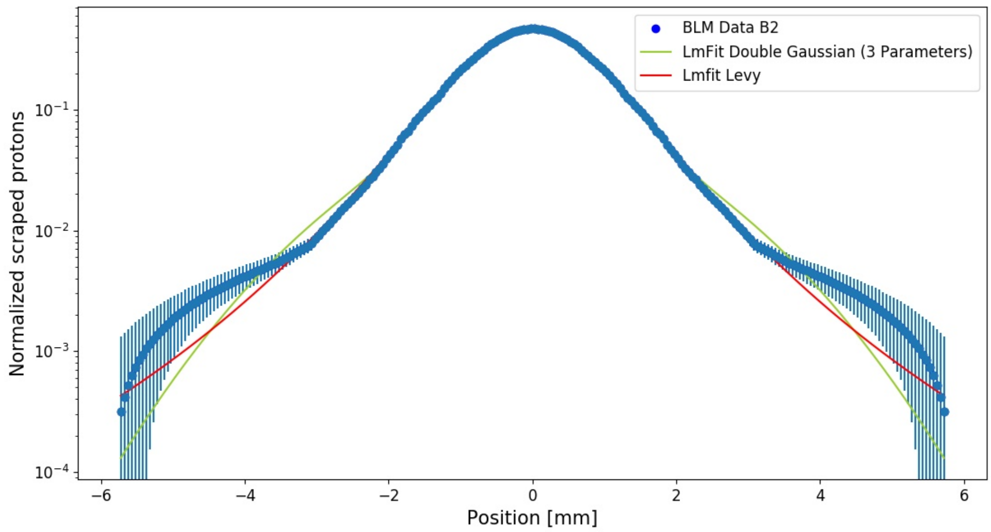

FIGURE 9.2: Horizontal scraping of B2 at injection and fitted profile, in logarithmic scale, using only the Lmfit library method.

The plots show the result of the scraping of B2, in the vertical plane, performed during 2018.

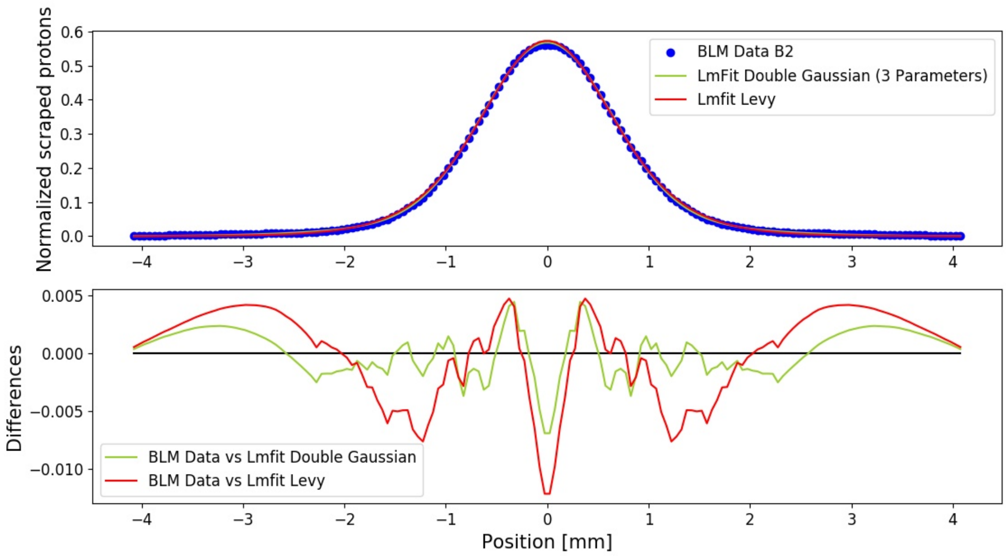

FIGURE 9.3: Vertical scraping of B2 at injection and fitted profile using only the Lmfit library method. The differences between the BLM data and the profile reconstructed with the Double Gaussian (green) and the Lèvy Student (red) models are also shown.

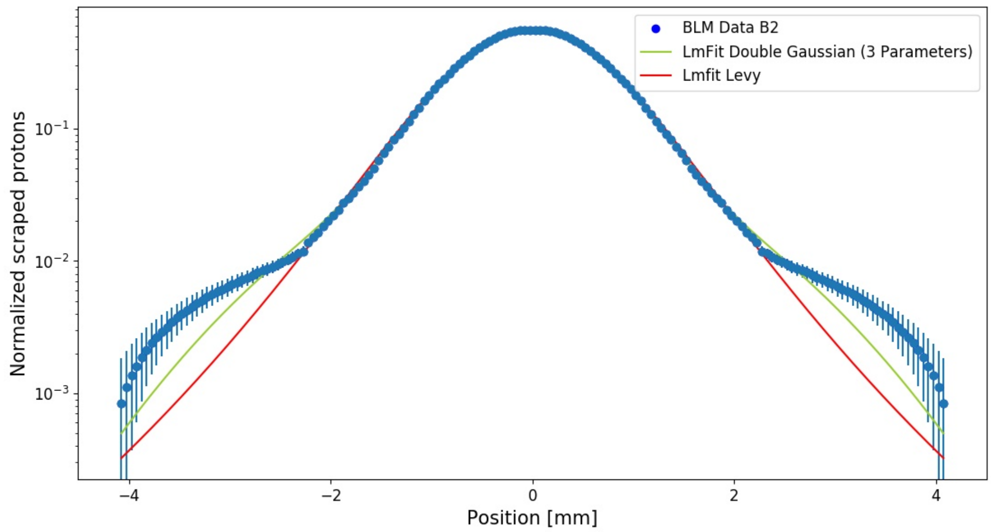

FIGURE 9.4: Vertical scraping of B2 at injection and fitted profile, in logarithmic scale, using only the Lmfit library method.

The plots show the result of the scraping of B2, in the skew plane, performed during 2018.

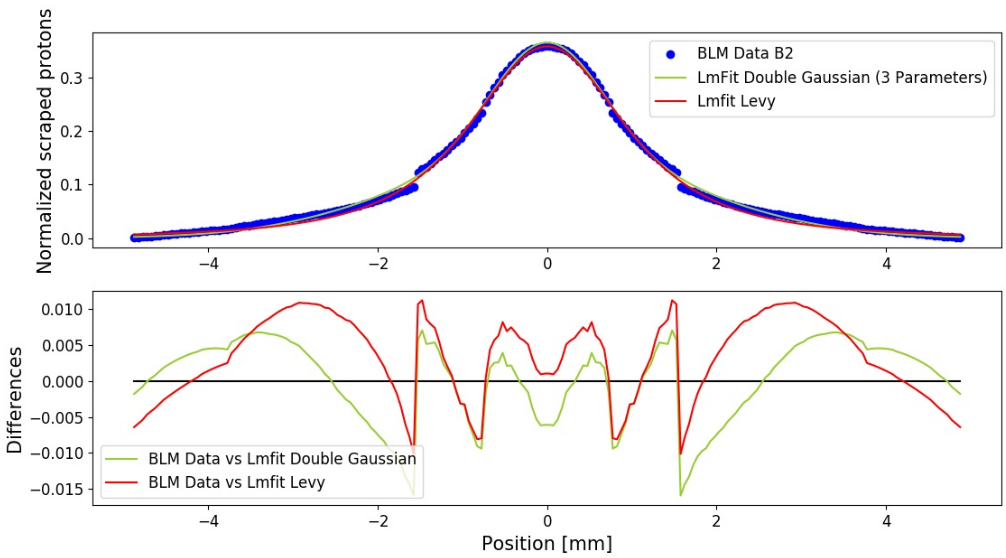

FIGURE 9.5: Skew scraping of B2 at injection and fitted profile using only the Lmfit library method. The differences between the BLM data and the profile reconstructed with the Double Gaussian (green) and the Lèvy Student (red) models are also shown.

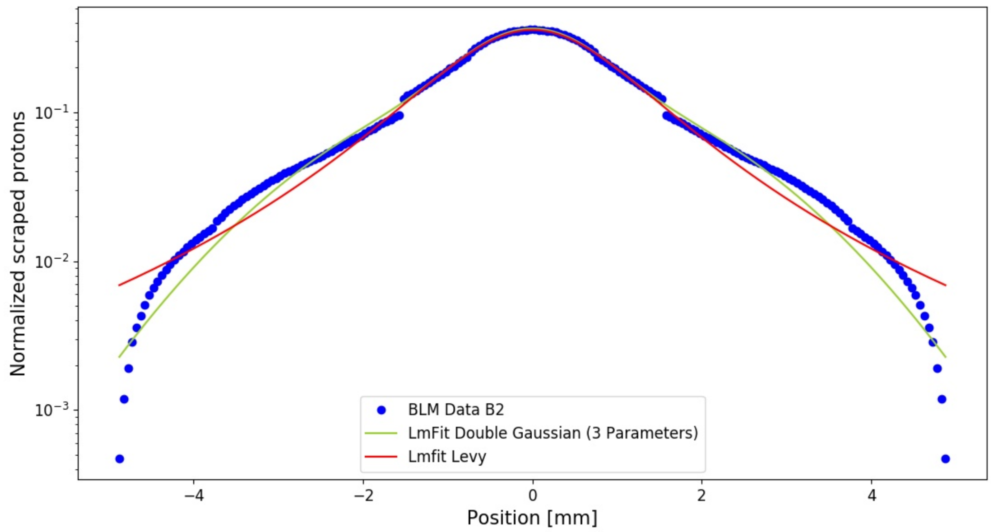

FIGURE 9.6: Skew scraping of B2 at injection and fitted profile, in logarithmic scale, using only the Lmfit library method.

The plots show the result of the scraping of B2, in the horizontal plane, performed during 2018.

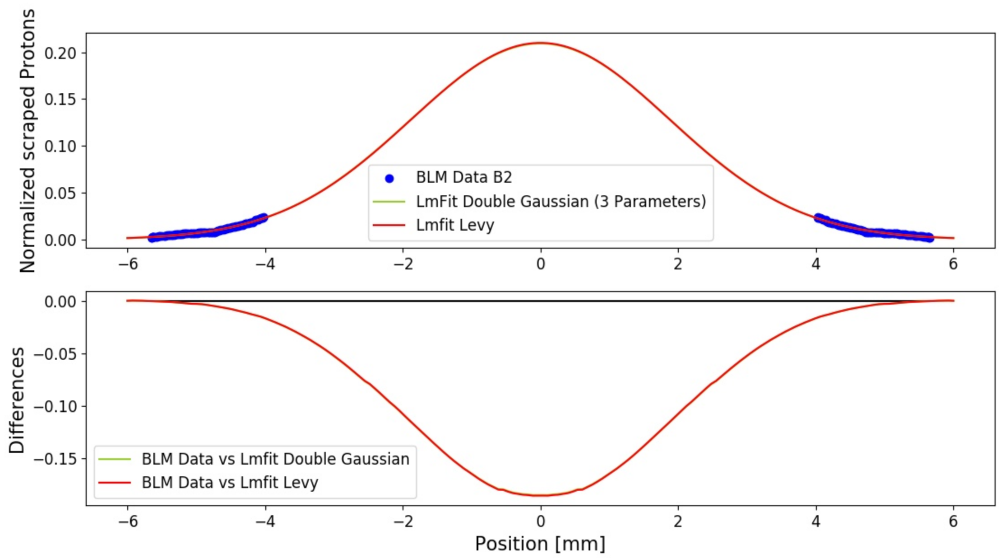

FIGURE 9.7: Horizontal scraping of B2 at injection and fitted profile using only the Lmfit library method. The differences between the BLM data and the profile reconstructed with the Double Gaussian (green) and the Lèvy Student (red) models are also shown.

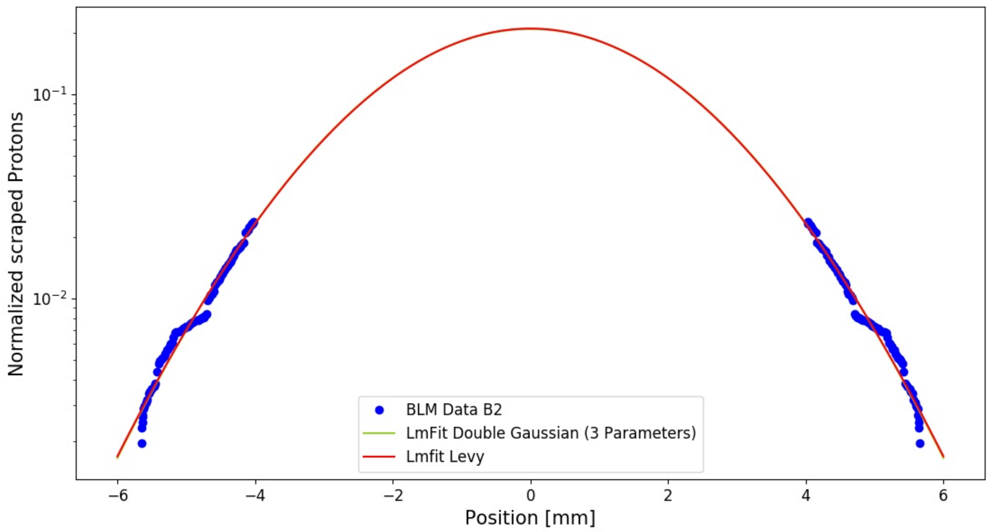

FIGURE 9.8: Horizontal scraping of B2 at injection and fitted profile, in logarithmic scale, using only the Lmfit library method.

9.2 Scraping at Flat Top

The plots show the result of the scraping of B2, in the vertical plane, performed during 2018.

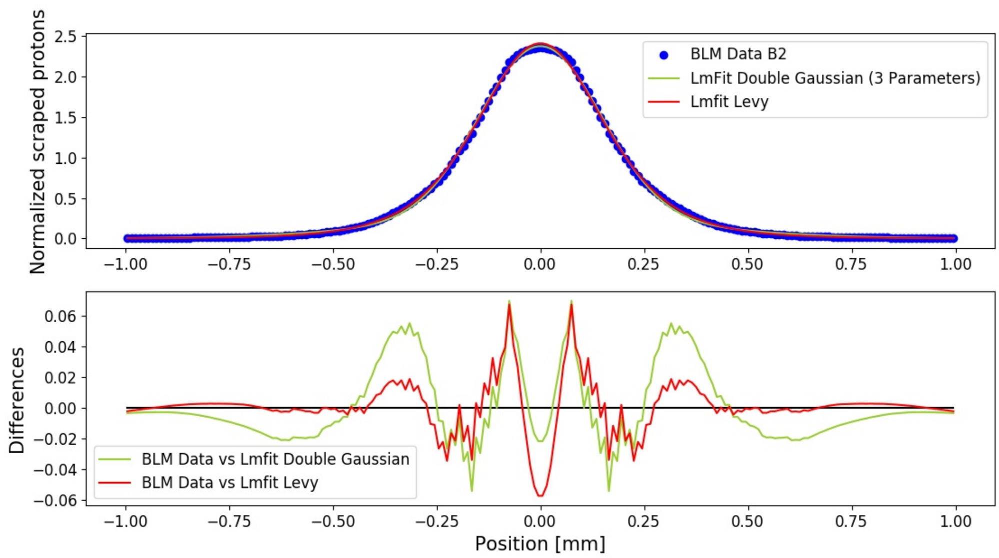

FIGURE 9.9: Vertical scraping of B2 at injection and fitted profile using only the Lmfit library method. The differences between the BLM data and the profile reconstructed with the Double Gaussian (green) and the Lèvy Student (red) models are also shown.

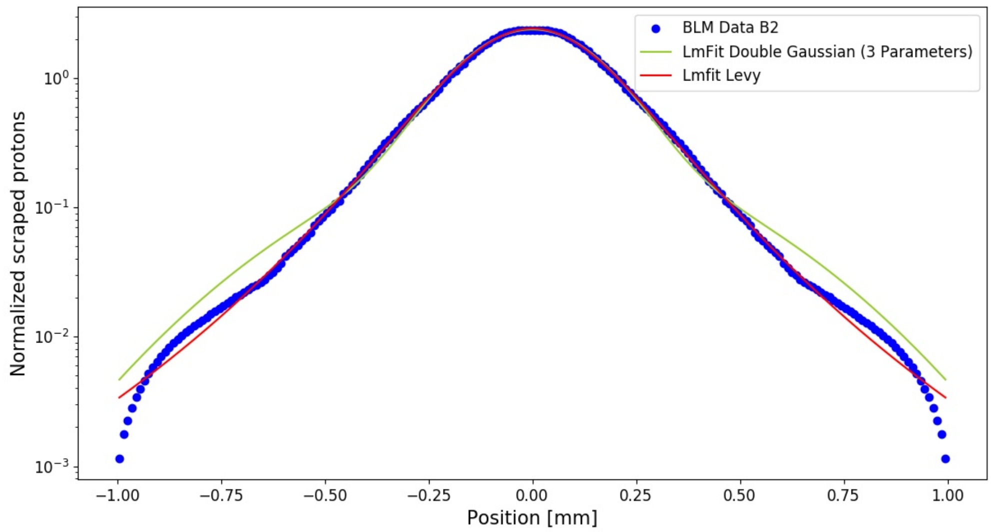

FIGURE 9.10: Vertical scraping of B2 at injection and fitted profile, in logarithmic scale, using only the Lmfit library method.

Bibliography

Appleby, R.B. et al. (2017). "Collimation System". In: *High-Luminosity Large Hadron Collider*. URL: https://www.researchgate.net/publication/317205286_Collimation_System.

Belohrad, D. (2010). "Fast Beam Intensity Measurements for the LHC". MA thesis. Czech Technical University in Prague.

Bracco, C. (2009). "Commissioning Scenarios and Tests for the LHC Collimation System". MA thesis. École Polytechnique Fèdérale De Lausanne.

Bravin, E. (2014). "Transverse beam profiles". In: *CERN Document Server*. URL: https://cds.cern.ch/record/1213283/files/p377.pdf.

Bruning, 0. et al. (2004). *LHC Design Report, Vol. I The LHC Main Ring*. Tech. rep. CERN European Organization For Nuclear Research.

Burkart, F. (2009). "Beam Loss and Beam Shape at the LHC Collimators". MA thesis. Institut Für Angewandte Physik Goethe Universität Frankfurt.

Burkart, F. et al. (2011). "HALO SCRAPINGS WITH COLLIMATORS IN THE LHC". In: *IPAC*. URL: https://www.researchgate.net/publication/254467769_Halo_scrapings_with_collimators_in_the_LHC.

Burkhardt, H. and R. Schmidt (2004). "INTENSITY AND LUMINOSITY AFTER BEAM SCRAPING". In: *CERN-AB-Note-2004-054 (ABP)*. URL: https://cds.cern.ch/record/777311/?ln=en.

Cheymol, B. (2011). "Development of beam transverse profile and emittance monitors for the CERN LINAC4". MA thesis. Université Clermont-Ferrand II - Blaise Pascal.

Dehning, B. et al. (2011). "Self Testing Functionality of the LHC BLM System". In: *CERN-BE-2011-025 BI*. URL: https://www.researchgate.net/publication/254199219.

Giovannozzi, M. (2012). "Proposed scaling law for intensity evolution in hadron storage rings based on dynamic aperture variation with time". In: *Physical Review*. URL: https://journals.aps.org/prab/pdf/10.1103/PhysRevSTAB.15.024001.

Herranz, J., A. Barjau, and B. Dehning (2016). "Vibration measurements of a wire scanner – experimental setup and models". In: URL: https://www.sciencedirect.com/science/article/pii/S0888327015003878.

Hostettler, M. et al. (2017). "HOW WELL DO WE KNOW OUR BEAMS?" In: *CERN Document Server*. URL: https://cds.cern.ch/record/2293521/files/1635044_119-124.pdf.

Kuhn, M. (2013). "Emittance Preservation at the LHC". MA thesis. University of Hamburg.

Lincoln, D. (2015). "Superconducting electromagnets of the LHC". In: *Symmetry*. URL: https://www.symmetrymagazine.org/article/january-2015/superconducting-electromagnets-of-the-lhc.

Maclean, E. H. (2014). "Modelling and correction of the non-linear transverse dynamics of the LHC from beam-based measurements". MA thesis. Herford College, University of Oxford.

Martino, S. De, S. De Siena, and F. Illuminati (2005). "Lévy-Student distributions for halos in accelerator beams". In: *PHYSICAL REVIEW*. URL: https://www.ba.infn.it/~cufaro/scientific/2005_PRE.pdf.

Redaelli, S. (2014). "Beam Cleaning and Collimation Systems". In: *Proceedings of the Joint International Accelerator School*. URL: https://www.researchgate.net/publication/306186620_Beam_Cleaning_and_Collimation_Systems.

Roncarolo, F. (2005). "Accuracy of the Transverse Emittance Measurements of the CERN Large Hadron Collider". MA thesis. Politecnico di Milano.

Wagner, J. F. et al. (2016). "FIRST ATTEMPTS AT USING ACTIVE HALO CONTROL AT THE LHC". In: *IPAC2016*. URL: https://www.researchgate.net/publication/303674204_FIRST_ATTEMPTS_AT_USING_ACTIVE_HALO_CONTROL_AT_THE_LHC.

Wikipedia. *Least Squares*. URL: https://en.wikipedia.org/wiki/Least_squares.

— *Simpson's rule*. URL: https://en.wikipedia.org/wiki/Simpson%27s_rule.

Wittenburg, K. (2013). "Specific instrumentation and diagnostics for high-intensity hadron beams". In: *CERN Yellow Report*. URL: https://arxiv.org/abs/1303.6767.